

Tropical and Stratospheric Influences on Extratropical Short-Term Climate Variability

Matthew Newman and Prashant D. Sardeshmukh

CIRES Climate Diagnostics Center, University of Colorado, and Physical Sciences
Division/NOAA Earth System Research Laboratory, Boulder, Colorado

Email: matt.newman@noaa.gov

Revision submitted to *Journal of Climate*

Friday, December 21, 2007

ABSTRACT

The relative impacts of tropical diabatic heating and stratospheric circulation anomalies on wintertime extratropical tropospheric variability are investigated in a linear inverse model (LIM) derived from the observed zero-lag and 5-day lag covariances of 7-day running mean departures from the annual cycle. The model predicts the covariances at all other lags. The predicted and observed lag-covariances are generally found to be in excellent agreement, even at the much longer lag of 21 days. This validates the LIM's basic premise that the dynamics of weekly averages are effectively linear and stochastically driven, and justifies further linear diagnosis of the system.

Analysis of interactions among the LIM's variables shows that tropical diabatic heating greatly enhances persistent variability over most of the Northern Hemisphere, especially over the Pacific and North America. Stratospheric effects are largely confined to the polar region, where they ensure that the dominant pattern of sea level pressure variability is the annular Arctic Oscillation rather than the more localized North Atlantic Oscillation. Over the North Atlantic, both effects are important, although some of the stratospheric influence is ultimately traceable to tropical forcing. In general, the tropically forced anomalies extend through the depth of the troposphere and into the stratosphere, whereas stratospherically generated anomalies tend to be largest at the surface and relatively weak at mid-tropospheric levels. Some persistent variability is, however, found even in the absence of these “external” forcings, especially near the amplitude maxima of the leading eigenmodes of the internal extratropical tropospheric evolution operator. One of these eigenmodes has a circumglobal zonal wavenumber-5 structure with maxima over the Arabian Sea and the central Pacific, and two others are associated with north-south dipole

variations across the North Atlantic jet. Overall, tropical influences are generally found to be larger than stratospheric influences on extratropical tropospheric variability, and to have a pronounced impact on the persistent, and therefore the potentially predictable, portion of that variability.

1. Introduction

Extratropical atmospheric variability on time scales longer than a week, often called “low-frequency” or short-term climate variability, is qualitatively different from daily synoptic variability. For example, during winter, synoptic variability is strongest in narrow regions north of the Atlantic and Pacific jets, whereas climate variability is largest in a broad region over the Northeast Pacific. Also, synoptic weather systems are typically zonally oriented, whereas climate anomalies occur as north-south dipoles or follow great circle paths. These differences appear on timescales as short as a week. Natural climate variability on longer timescales is not fundamentally different from weekly variability, although it can differ in details (e.g., Kushnir and Wallace 1989; Feldstein 2000).

It is often suggested that climate variability reflects barotropic energy dispersion in a spherical atmosphere (Hoskins and Karoly 1981; Simmons 1982) in which anomalies are strongly influenced by the time-mean ambient flow (e.g., Simmons et al. 1983). Although this hypothesis was originally proposed in terms of the modal instability of the ambient flow, subsequent studies stressed energy extraction in preferred regions followed by propagation along preferred ray paths (e.g., Hoskins and Ambrizzi 1993; Borges and Sardeshmukh 1995; Branstator and Frederikson 2003). In such a scenario, some source of initial perturbations is needed, although substantial transient anomaly growth is still possible. The simplest model incorporating this may be expressed as

$$(1) \quad \frac{d\mathbf{x}}{dt} = \mathbf{L}\mathbf{x} + \mathbf{F},$$

where \mathbf{x} is a state vector representing extratropical tropospheric climate anomalies, \mathbf{L} is a linear dynamical operator which includes base-state interactions, and \mathbf{F} represents

forcing. For (1) to be a closed system, \mathbf{F} can represent only stochastic forcing with externally specified amplitudes; otherwise a second model of \mathbf{F} would be needed.

Such a simple model can reproduce the gross features of observed low-frequency variance statistics if \mathbf{L} is a linearized barotropic operator (e.g., Egger and Schilling 1983; Newman et al. 1997; Branstator and Frederikson 2003). However, as Newman et al (1997) stressed, it does a poor job of explaining the *evolution* of climate anomalies and related statistics such as lag-covariances. In particular, a linear barotropic model of the form (1) is a poor forecast model of short-term climate anomalies, worse than even persistence (Sardeshmukh et al 1997; Winkler et al 2001). The reason for this is simple: the free barotropic eigenmodes have a relatively narrow range of decay rates but a wide range of phase speeds (e.g., Fig. 2 of Newman et al.). A random forcing causes all the modes to be excited roughly equally on average, but their subsequent rapid dispersion leads to unrealistically small lag-covariances. For (1) to produce realistic lag-covariances in a barotropic framework, there has to be a process (for example, a part of \mathbf{F}) that is not random, but rather acts to select some slowly evolving modes preferentially over others.

There are several ways to improve on the barotropic model while retaining the basic form of (1), although modified barotropic (Cai and van den Dool 1991; Mitas and Robinson 2005) and simple baroclinic (Winkler et al. 2001) models have not proved much more successful in this regard. One possibility is to include linear synoptic eddy feedbacks (e.g., Lau 1988; Branstator 1995; Whitaker and Sardeshmukh 1998) in \mathbf{L} , which, given that they are generally positive (Valdes and Hoskins 1989), would have a destabilizing effect on the lower-frequency eigenmodes of \mathbf{L} , making their selection easier. A second possibility is for \mathbf{F} to include non-random “external” forcings of the extratropical

tropospheric circulation, such as from the tropics and stratosphere. If these “forcings” are not entirely independent of \mathbf{x} and/or each other, however, then one would need a linear model of the form (1), including linear interactions with other system components, for these “forcings” as well. In effect, one would then have a combined model of the form (1) for an augmented state vector \mathbf{x} that includes these “forcings” as additional components, but with \mathbf{F} now again strictly random.

There is, of course, also the possibility that the *form* (1) itself is incorrect; especially given the suggestion of nonlinear low-frequency behavior (e.g., Kimoto and Ghil 1993; Corti et al 1999). The dynamics of some nonlinear systems with “slow” and “fast” components can, however, be approximated by linear deterministic dynamics plus stochastic white noise forcing if the nonlinearities decorrelate sufficiently rapidly relative to the time scales of forecast interest (e.g., Papanicolaou and Kohler 1974; Hasselmann 1976; Penland 1996). In such systems, the predictable parts of future states are associated with purely linear and/or linearly parameterizable dynamics, so the system is *effectively* linear (Newman et al. 2003) and can be approximated by (1) with $\mathbf{F} = \boldsymbol{\xi}$ as a white noise forcing (which may or may not have geographical structure). In Part I of this work (Winkler et al. 2001; hereafter WNS) we derived such an effectively linear dynamical model from observations. The model was shown to have good forecast skill (WNS; Newman et al. 2003), and predictability estimates derived from it were shown to be consistent both with its own actual forecast skill and, more important, with that of a (bias-corrected) version of the medium-range forecast model used operationally at NCEP in 1998 (Newman et al. 2003).

Many previous studies have considered either tropical or stratospheric influences on extratropical tropospheric variability, but generally not both. For example, the state vector considered by WNS (including weekly extratropical tropospheric streamfunction and tropical diabatic heating anomalies) did not allow an evaluation of the relative importance of the tropical and stratospheric influences. This is increasingly becoming an important issue given, for example, the evidence of both tropical (Sardeshmukh et al. 2000; Hoerling et al. 2001; Lin et al. 2002; Branstator 2002; Zhou and Miller 2005; Bader and Latif 2005) and stratospheric (Baldwin and Dunkerton 2001; Ambaum and Hoskins 2002; Thompson et al. 2002) influences on the North Atlantic Oscillation (NAO). There is also some recent evidence that observed stratospheric variability is related to ENSO (e.g., Camp and Tung 2007; Wei et al. 2007) and that such variability can be reproduced by GCMs with prescribed observed sea surface temperatures (e.g. Lahoz 2000; Taguchi and Hartmann 2006; Manzini et al. 2006). This raises the possibility that at least some extratropical tropospheric effects previously attributed to stratospheric influences may ultimately be traceable to tropical forcing. On the other hand, some stratospheric influences may also have been implicitly included in WNS's empirically derived \mathbf{L} operator, possibly leading to an overstatement of tropical influences in their study.

Our principal aim in this paper is thus to compare the impacts of tropical heating and stratospheric circulation anomalies on short-term extratropical tropospheric climate variability, including that at the surface, in a single dynamical framework. To this end we will extend the LIM of WNS by including stratospheric streamfunction and sea level pressure as part of the model state vector, as described in section 2. We consider an explicit treatment of sea level pressure to be important, given the evidence in several

studies that stratospheric-tropospheric connections are more pronounced at the surface than at mid-tropospheric levels (e.g., Baldwin et al. 2003; Thompson et al. 2006). In section 3, we show that our extended LIM’s forecast skill is as good or better than that of WNS’s LIM. As a further key demonstration of linearity justifying our linear diagnosis here, we show that the LIM reproduces the observed lag-covariances at much longer lags than the lag at which it is trained. In section 4, both tropical diabatic heating and stratospheric influences are shown to be crucial for this successful reproduction, although the tropical effect is dominant over the Pacific sector and throughout the mid-troposphere, whereas stratospheric effects are largest at the surface of the Arctic and, apart from the North Atlantic, are less significant elsewhere. More detailed diagnosis of the differing tropical and stratospheric impacts on tropospheric anomaly amplification and forecast skill is presented in section 5. Diagnosis of tropical impacts upon stratospheric variability is presented in section 6. Some issues relating to the LIM’s relatively poor performance at the surface over some of the North Atlantic are discussed in section 7, and concluding remarks are made in section 8.

2. Model details and data

The model state vector \mathbf{x} in (1) is

$$\mathbf{x} = \begin{bmatrix} \mathbf{p} \\ \boldsymbol{\Psi}_T \\ \mathbf{H} \\ \boldsymbol{\Psi}_S \end{bmatrix}$$

where \mathbf{p} is sea-level pressure (SLP), $\boldsymbol{\Psi}_T$ is tropospheric streamfunction, \mathbf{H} is tropical diabatic heating, and $\boldsymbol{\Psi}_S$ is stratospheric streamfunction. All quantities represent 7-day

running mean anomalies. Thirty-five years (1968/69 to 2002/03) of wintertime (December 1—February 28) NCEP-NCAR Reanalysis data were used to define \mathbf{x} . The diabatic heating rates were determined from an improved iterative solution of the “chi-problem” (Sardeshmukh 1993; Sardeshmukh et al. 1999), as described in WNS. All variables were spectrally truncated to T21 and transformed onto a Gaussian grid; this truncation affects none of our results. Low-frequency anomalies were defined by removing each variable’s annual cycle, defined by running a 31-point smoother on the daily climatology of the lowpass data, at each gridpoint from the weekly means. Constructing anomalies in this manner gave virtually identical results to the slightly different method used by WNS. Tropospheric streamfunction anomalies ψ_T were determined at 250 hPa (ψ_{250}) and 750 hPa (ψ_{750}), and stratospheric streamfunction anomalies ψ_S at 30 hPa; similar results (not shown) were obtained by defining ψ_S at 70 hPa. Diabatic heating anomalies were smoothed using a T21 spectral filter that attenuates small-scale features and Gibbs phenomena (Sardeshmukh and Hoskins 1984).

The anomaly fields were projected onto their leading Empirical Orthogonal Functions (EOFs). As in WNS, all EOFs were determined for the Northern Hemisphere (NH) except for diabatic heating EOFs, which were determined for the region 30°S—30°N. Prior to computing EOFs, each anomaly field was normalized by its domain-averaged climatological root-mean-square amplitude. The EOFs of tropospheric streamfunction were computed from a vector combining the normalized ψ_{250} and ψ_{750} anomalies rather than at each level separately. Figure 1 shows the leading two EOFs of ψ_T (displayed only at 250 hPa), \mathbf{p} , ψ_S , and \mathbf{H} , and the fractional variances of these fields explained by them. The EOFs of ψ_T and \mathbf{H} are essentially the same as in WNS. The leading \mathbf{p} EOF, or

$\mathbf{p}/\text{EOF1}$, shows the well-known Atlantic pattern variously termed the North Atlantic Oscillation (NAO; e.g., Deser 2000; Ambaum et al. 2001) or the Arctic Oscillation (AO; e.g., Thompson and Wallace 2000). It is often also referred to as an “annular mode”, but at least for 7-day means this EOF has a strong wavenumber-1 component. The $\boldsymbol{\psi}_S/\text{EOF1}$ is strongly associated with the quasi-biennial oscillation (QBO), including relatively strong zonally symmetric zonal wind anomalies in the Tropics and around 70°N (Holton and Tan 1982; Randel et al. 1999), and a corresponding principal component dominated by (though not exclusively comprising) variations of roughly two-year period. Note that the patterns in Fig. 1 do not represent EOFs of the combined fields; so, for example, $\boldsymbol{\psi}_T/\text{EOF1}$ corresponds best to $\mathbf{p}/\text{EOF2}$, and $\mathbf{p}/\text{EOF1}$ corresponds best to $\boldsymbol{\psi}_T/\text{EOF4}$ (not shown).

The leading 40/24/18/4 EOFs of $\boldsymbol{\psi}_T/\mathbf{p}/\mathbf{H}/\boldsymbol{\psi}_S$ were retained, explaining about 90/90/55/84 percent of the variability of these fields. The time-varying coefficients of these EOFs, i.e. the principal components (PCs), define our 86-component state vector \mathbf{x} . Note that we retain substantially more tropical diabatic heating variance than did WNS because we did not encounter the Nyquist-lag problem encountered by them, possibly because of our use of 4x daily data as opposed to their use of 2x daily data. As in WNS, a training lag of $\tau_0 = 5$ days was used to estimate \mathbf{L} from the relationship $\mathbf{C}(\tau_0) = \exp(\mathbf{L}\tau_0) \mathbf{C}(0)$, where $\mathbf{C}(\tau) = \langle \mathbf{x}(t+\tau)\mathbf{x}^T(t) \rangle$. The EOF truncations and training lag were chosen to maximize the LIM’s cross-validated forecast skill (see below and WNS). In no other respect do our choices of training lag and EOF truncations affect the points made in this paper. Minor sensitivities of the results to these choices were similar to those reported in WNS, and so are not repeated here.

3. Evaluating the LIM

Figure 2 (right panels) shows the LIM's forecast skill, measured in terms of local anomaly correlation between the untruncated observations and the Week 3 forecasts of ψ_{250} and \mathbf{p} that were cross-validated (i.e. verified on independent data) as described in WNS. The full LIM's skill in Figure 2 is similar to that of WNS's LIM. Extending the LIM's state vector with \mathbf{p} and ψ_S components improves neither ψ_T nor \mathbf{H} skill (not shown, but see Newman et al. 2003), as is clear from comparison with a LIM derived from ψ_T and \mathbf{H} alone (" ψ_T/\mathbf{H} LIM"; cf. Fig. 2a to 2b) as in WNS. On the other hand, a " \mathbf{p}/ψ_S LIM" derived from \mathbf{p} and ψ_S alone is generally much less skillful than the full LIM at forecasting \mathbf{p} (cf. Figs. 2c and 2d). The exception is over the polar and North Atlantic regions. Most of the polar \mathbf{p} skill is due to ψ_S : for LIMs constructed *without* ψ_S (not shown), polar \mathbf{p} skill is only ~ 0.15 (except 0.3 around 30°E). This result is consistent with earlier studies of statistical surface forecast skill dependence upon the stratosphere where the predictand was either the AO (Baldwin et al. 2003; Charlton et al. 2003) or zonal mean zonal wind at 60°N (Christiansen 2005). On the other hand, most of the North Atlantic \mathbf{p} skill can also be obtained from a LIM constructed from \mathbf{p} alone (not shown).

WNS showed that their LIM could reproduce a broad measure of lagged covariance, the trace of the lag-autocovariance matrix (proportional to the lag-autocovariance averaged over all PCs), for lags up to 30 days. In the following, we perform a more detailed comparison of the predicted and observed lag-autocovariances in grid space. This is a key test of linearity, since (1) implies that $\mathbf{C}(\tau) = \mathbf{G}(\tau) \mathbf{C}(0)$, with $\mathbf{G}(\tau) = \exp(\mathbf{L}\tau)$.

Figure 3 compares the observed 21-day lag-autocovariances of ψ_{250} and \mathbf{p} with the LIM's predicted values. The results for ψ_{750} are intermediate between those for the surface and

250 hPa, and are therefore not shown. The LIM's prediction is best at 250 hPa (top panels of Fig. 3), especially over the Pacific. The relatively minor differences over the Atlantic are well within sampling uncertainty (see section 7). These errors are very small compared to the corresponding errors of a two-level linear balance model described in WNS, which produces weak *negative* 21-day lag-autocovariances throughout the hemisphere (not shown). The LIM's predicted lag-autocovariances of **p** (middle panels of Fig. 3) are also realistic over the Pacific, although the observed region of high persistence extends about 10° farther west. The LIM captures the locations and amplitudes of all other extrema with the clear exception of the **p** maximum over the North Atlantic. This difference is apparently unrelated to discrepancies in the LIM's stratospheric (not shown) and tropical heating lagged auto-covariances (bottom panels of Fig. 3), which are rather small apart from an underestimation of tropical heating persistence in the central equatorial Pacific (but see section 7). In fact, tropical heating is critical to the LIM's success here: only LIMs that include **H** can reproduce the observed magnitude of extratropical lag-autocovariance for lags greater than two weeks.

Regions of relatively large lag-autocovariance also tend to be regions of persistent anomalies, and therefore of relatively large low-frequency variance. One can make a more direct comparison of the LIM's predicted low-frequency variance with observations, either by computing the power in desired frequency bands directly from (1) as in Penland and Ghil (1993), or by making a long run of (1) and collecting statistics. We followed the latter approach, integrating (1) forward for 50000 days using the method described in Penland and Matrosova (1994). The white noise forcing $\xi = \sum_j \mathbf{q}_j \boldsymbol{\eta}_j r_j(t)$ was specified using independent Gaussian white noises $r_j(t)$ with unit variance, and \mathbf{q}_j and $(\boldsymbol{\eta}_j)^2$ as the

eigenvectors and eigenvalues, respectively, of the positive-definite noise covariance matrix $\mathbf{Q} = \langle \xi \xi^T \rangle dt$, estimated using the Fluctuation-Dissipation relationship,

$$(2) \quad d\mathbf{C}(0)/dt = \mathbf{0} = \mathbf{L}\mathbf{C}(0) + \mathbf{C}(0)\mathbf{L}^T + \mathbf{Q},$$

to solve for \mathbf{Q} given the observed $\mathbf{C}(0)$ and \mathbf{L} . This solution is guaranteed to be symmetric but not positive-definite. Indeed we found four small negative eigenvalues of \mathbf{Q} accounting for less than 1% of the trace of \mathbf{Q} . Following Penland and Matrosova (1994), we produced a legitimate modified noise covariance matrix by setting those negative eigenvalues to zero, rescaling the remaining positive eigenvalues to preserve the total forcing variance, and reconstructing \mathbf{Q} using the rescaled eigenvalues and corresponding eigenvectors. This reconstruction resulted in an increase of noise variance just southeast of Greenland. Finally, a modified $\mathbf{C}(0)$ consistent with (1) was recalculated from (2) by specifying \mathbf{L} and the modified \mathbf{Q} . The impact of this modification was small, as can be seen by comparing the observed (top) and modified (middle) Ψ_{250} variance maps in the left panels of Fig. 4. Note that these would be identical (apart from the EOF truncation) if \mathbf{Q} had not been modified.

We constructed 21-day running means from the long LIM model run by averaging sets of three values each spaced seven days apart. The resulting comparison of LIM-predicted variance of 21-day means to the observed variance of 21-day means (right panels of Fig. 4) is encouraging because it is a harder test for the LIM than the comparison of total variance, since it tests the spectral distribution of the variance i.e the fidelity of the simulated power spectrum.

4. Tropical and stratospheric influences on persistent variability

Following the approach of Newman et al. (2000), the relative importance of tropical heating and stratospheric influences in extratropical tropospheric dynamics may be investigated in a framework in which (1) is rewritten as

$$(3) \quad \frac{d}{dt} \begin{bmatrix} \mathbf{x}_T \\ \mathbf{H} \\ \boldsymbol{\psi}_S \end{bmatrix} = \begin{bmatrix} \mathbf{L}_{TT} & \mathbf{L}_{TH} & \mathbf{L}_{TS} \\ \mathbf{L}_{HT} & \mathbf{L}_{HH} & \mathbf{L}_{HS} \\ \mathbf{L}_{ST} & \mathbf{L}_{SH} & \mathbf{L}_{SS} \end{bmatrix} \begin{bmatrix} \mathbf{x}_T \\ \mathbf{H} \\ \boldsymbol{\psi}_S \end{bmatrix} + \begin{bmatrix} \boldsymbol{\xi}_T \\ \boldsymbol{\xi}_H \\ \boldsymbol{\xi}_S \end{bmatrix}$$

where \mathbf{x}_T represents the tropospheric circulation subvector, which now includes $\boldsymbol{\psi}_T$ and \mathbf{p} .

Note that \mathbf{L}_{TT} is distinct from a linear operator (say, $\hat{\mathbf{L}}_{TT}$) obtained from a LIM of \mathbf{x}_T alone. The latter would implicitly include linear diagnostic relationships between \mathbf{x}_T and \mathbf{H} and $\boldsymbol{\psi}_S$. By explicitly separating out the effects of \mathbf{H} and $\boldsymbol{\psi}_S$ on \mathbf{x}_T , (3) enables us to identify \mathbf{L}_{TT} more cleanly with “internal” extratropical tropospheric dynamics. Of course, \mathbf{L}_{TT} may still implicitly retain the influence of variables not included in \mathbf{x} .

To make an overall assessment of the “external” tropical heating and stratospheric influences on extratropical tropospheric variability, we made another 50000-day run, of the system

$$(4) \quad \frac{d\mathbf{x}_T}{dt} = \mathbf{L}_{TT}\mathbf{x}_T + \boldsymbol{\xi}_T .$$

The bottom left panel of Fig. 4 shows the variance of $\boldsymbol{\psi}_{250}$ obtained in this run. As expected, removing the external influences decreases the variance, although this change is generally far smaller over the Atlantic than the Pacific. Similar results are obtained for \mathbf{p} (not shown). Removing the external influences has a larger impact on the variance of

the 21-day means, as shown in the bottom right panel of Fig. 4. However, the impacts over the central Pacific and North Atlantic remain small even at these longer time scales.

Further isolation of the tropical heating and stratospheric influences is possible by considering two modified \mathbf{L} operators : \mathbf{L}_{noh} , in which $\mathbf{L}_{TH} = \mathbf{L}_{HT} = \mathbf{L}_{SH} = \mathbf{L}_{HS} = 0$; and \mathbf{L}_{nos} , in which $\mathbf{L}_{TS} = \mathbf{L}_{ST} = \mathbf{L}_{HS} = \mathbf{L}_{SH} = 0$. The predicted lag-covariances using these modified operators are $\mathbf{C}_{\text{noh}}(\tau) = \exp(\mathbf{L}_{\text{noh}}\tau)\mathbf{C}(0)$ and $\mathbf{C}_{\text{nos}}(\tau) = \exp(\mathbf{L}_{\text{nos}}\tau)\mathbf{C}(0)$. Results for the 21-day lag auto-covariances are shown in Fig. 5. For reference, the top panels repeat the full LIM's predictions for $\boldsymbol{\psi}_{250}$ (left) and \mathbf{p} (right) from Fig. 3. The much weaker lag covariance obtained without tropical heating (middle panels) shows that the heating is responsible for most of the observed persistent variability over most of the domain, whereas the stratospheric impact (bottom panels) is generally minor. At the surface over the North Atlantic and polar regions, however, the picture is more mixed, with tropical heating responsible for much of the persistence over the far North Atlantic but the stratosphere responsible for about half of the persistence in the Arctic north of Siberia, near the positive center of \mathbf{p} /EOF1 (cf. Fig. 1). At longer lags such as 35 days (not shown) over the far North Atlantic, the stratospheric impact increases to equal that of tropical heating.

Although removing these external influences generally diminishes the persistence of extratropical tropospheric anomalies, some persistence remains, especially over the Atlantic and near the dateline in the Pacific (see bottom right panel of Fig.4 and middle left panel of Fig.5). This persistence cannot be captured by a stochastically forced 2-level linear balance model of extratropical dynamics (not shown). It is, however, linked to the least damped eigenmodes of our empirically determined “internal” extratropical

dynamical operator \mathbf{L}_{TT} . For example, the pattern of persistence over the Atlantic is consistent with the structures of the two leading eigenmodes of \mathbf{L}_{TT} , shown in Figs. 6a and 6b for ψ_{250} (other levels not shown). Both modes are stationary north-south dipoles straddling the Atlantic jet, with e-folding decay times of about three weeks (much shorter than for the leading eigenmodes of the full \mathbf{L} operator); the first tilts westward with height and the second, which strongly resembles the NAO at the surface, is barotropic. These Atlantic eigenmodes are quite different from the leading eigenmodes of simple barotropic or baroclinic models linearized about the time-mean basic state. This suggests that synoptic eddy feedbacks, which are in effect parameterized in \mathbf{L}_{TT} , modify those eigenmodes so as to enhance persistence, primarily over the Atlantic.

The most energetic phase of the third eigenmode of \mathbf{L}_{TT} , with maximum amplitude in the Pacific sector, is a circumglobal pattern (Fig. 6c) similar to that in Branstator (2002) except for relatively weak amplitude in the North Atlantic. It is remarkable how well the amplitude maxima of this circumglobal mode match the maxima of the simulated persistent variability without external tropical and stratospheric influences (cf. Fig. 6c to the bottom right panel of Fig. 4 and middle left panel of Fig. 5). The least energetic phase of this eigenmode (not shown), a weak zonally elongated north-south dipole straddling the west Pacific jet, is effectively distinct from the circumglobal pattern since the eigenmode has a 200-day period, longer than three e-folding times. Unlike in Fig. 6b, there is no dipole mode straddling the Pacific jet exit.

It is interesting that no single eigenmode of the full \mathbf{L} operator can be identified with the unforced circumglobal mode, although a few eigenmodes (not shown) do have maxima in some of the same locations. Perhaps the closest is the fourth eigenmode, whose tropical

heating component resembles the **H**/EOF2 and whose extratropical structure combines aspects of the unforced circumglobal mode (Fig. 6c) with the second unforced Atlantic mode (Fig. 6b). This fourth mode is also very similar to a pattern obtained by regressing winter-mean upper level streamfunction anomalies on the leading principal component of low-level North Atlantic streamfunction anomalies (Branstator 2002).

The tropospheric covariance budget, which may be expressed using (2) and (3) in the form

$$(5) \quad [\mathbf{L}_{TT}\mathbf{C}_{TT} + \mathbf{C}_{TT}\mathbf{L}_{TT}^T] + [\mathbf{L}_{TH}\mathbf{C}_{HT} + \mathbf{C}_{TH}\mathbf{L}_{TH}^T] + [\mathbf{L}_{TS}\mathbf{C}_{ST} + \mathbf{C}_{TS}\mathbf{L}_{TS}^T] + \mathbf{Q}_{TT} = \mathbf{O},$$

Internal Tropospheric Tropical Heating Stratospheric Stochastic

where $\mathbf{C}_{xy} = \langle \mathbf{xy}^T \rangle$, provides an alternative method of isolating the importance of tropical and stratospheric influences on extratropical tropospheric variability. Figure 7 shows the diagonal elements corresponding to ψ_{250} of each of the bracketed terms in this budget, which may be interpreted as their contribution to the local ψ_{250} variance tendency. It should be kept in mind that although these terms relate to the maintenance of local variance, they contain non-local effects: \mathbf{L}_{TT} and \mathbf{C}_{TT} are not diagonal matrices, and tropical heating and stratospheric circulation variability contribute to tropospheric streamfunction variability. The primary balance in Fig.7 is between the stochastic noise forcing, which acts to maintain the variance, and the internal tropospheric dynamical terms, whose net effect is to dissipate it (hence "Fluctuation-Dissipation"). Over most of the hemisphere, the tropical heating generates less variance than the noise forcing, except in Rossby wave source regions in the subtropics (Sardeshmukh and Hoskins 1988). The stratospheric influence is again generally small. Similar results are obtained for the SLP

variance (not shown), except that the stratospheric effect is slightly stronger and has centers over Scandinavia, Greenland, and Siberia.

It is interesting to break down the internal tropospheric term in Fig. 7 further into “local” and “non-local” contributions. The local contribution is associated with the product of the diagonal elements of \mathbf{L}_{TT} with the corresponding diagonal elements of \mathbf{C}_{TT} , and the non-local contribution with the difference of the local contribution from the total internal tropospheric term. As expected, the local contribution is dissipative, with an e-folding decay time scale ranging from ~ 3.5 days over land and the far western Pacific to ~ 5 days over the oceans, except for ~ 6 days over the far North Atlantic and Arctic oceans (cf. Fig. 4). The non-local term, generally positive owing to the destabilization of low-frequency anomalies through interactions with the time-mean basic state (e.g., Simmons et al. 1983; Borges and Sardeshmukh 1995) as well as positive synoptic-eddy feedbacks (Valdes and Hoskins 1989, Whitaker and Sardeshmukh 1998), offsets the local dissipation, but falls well short of overcoming it.

5. Tropical and stratospheric influences on rapidly amplifying structures

To better understand the results of the previous section, it is useful to examine tropical and stratospheric influences on the evolution of large-amplitude and long-lasting tropospheric anomalies. To this end we consider the singular vector decomposition (SVD) of the system propagator $\mathbf{G}(\tau) = \exp(\mathbf{L}\tau)$, under various norms and lead times τ , which yields a dominant pair $\mathbf{u}_1, \mathbf{v}_1$ of normalized singular vectors associated with the maximum singular value λ_1 (e.g., Farrell 1988; Sardeshmukh et al 1997). This identifies the “optimal” initial condition \mathbf{v}_1 leading to the largest anomaly $\mathbf{G} \mathbf{v}_1 = \lambda_1 \mathbf{u}_1$ at time τ (under a chosen norm). Newman et al. (2003) suggested that weekly extratropical

anomalies should be most predictable when there is a large initial projection on \mathbf{v}_1 . The maximum possible anomaly growth factors λ_1^2 , determined separately for each model variable in the L2 norm (i.e., domain-mean square amplitude), are displayed as functions of τ in Fig. 8 as “maximum amplification” (MA) curves (Penland and Sardeshmukh 1995). The results for $\boldsymbol{\psi}_T$ are qualitatively similar to those found earlier by WNS, but since our system is higher-dimensional than in WNS, it has the potential for larger amplification. Note that the peak in the MA curve occurs earlier for \mathbf{p} than for $\boldsymbol{\psi}_T$, suggesting that the predictability of \mathbf{p} might also peak earlier than that of $\boldsymbol{\psi}_T$, which is consistent with the lower 21-day \mathbf{p} forecast skill (Fig. 2).

These different curves also correspond to the different optimal initial and final states associated with the maximum possible growth of each model variable. For example, maximizing the amplification of $\boldsymbol{\psi}_T$ /EOF1 over a 21-day interval requires an optimal initial condition dominated by large tropical heating anomalies, as WNS earlier found for growth under the global $\boldsymbol{\psi}_T$ norm. In fact, the response to just the initial tropical anomaly in our case, shown in the left panels of Fig. 9, is only somewhat weaker than the response to the full optimal initial condition (not shown). On the other hand, maximizing the amplification of \mathbf{p} /EOF1 requires a very different initial condition, including larger initial stratospheric polar and tropospheric North Atlantic anomalies (not shown). In this case, the 21-day response is mostly due to the extratropical portion of the optimal initial condition (right panels of Fig. 9). Tropical heating plays a secondary role in the growth of \mathbf{p} /EOF1 for leads this short. Note that maximizing the amplitude of \mathbf{p} / EOF1 does not result in a correspondingly large mid-tropospheric anomaly. In general, we find that large

amplification of surface anomalies tends to occur with relatively weaker mid-tropospheric amplification, and vice versa.

Obviously, the atmosphere does not care which norm we choose. However, when making a forecast, some variables may be of more interest than others, in which case initial conditions leading to large anomalies in those variables become of interest. The choice of norm is then no longer arbitrary, and an SVD analysis of \mathbf{G} under that norm can provide valuable insight into potential forecast skill. For example, amplification (and potential predictability) of $\boldsymbol{\psi}_T$ is potentially larger than of \mathbf{p} (Fig. 8). Likewise, Fig. 10 shows that the cross-validated anomaly correlation skill of LIM forecasts, for leads up to 30 days, is generally higher for the leading PCs of $\boldsymbol{\psi}_T$ than for the leading PCs of \mathbf{p} .

Also shown in Fig. 10 is the skill of forecasts in which the initial anomalies of either \mathbf{H} or $\boldsymbol{\psi}_S$ are set to zero. Note that this is not quite the same as making forecasts using the modified operators \mathbf{L}_{noh} and \mathbf{L}_{nos} discussed in section 4, since the full LIM used here can subsequently generate \mathbf{H} and/or $\boldsymbol{\psi}_S$ anomalies that subsequently affect other forecast variables. In other words, instead of assessing the effect of entirely removing tropical or stratospheric influences, we determine how a large initial \mathbf{H} or $\boldsymbol{\psi}_S$ anomaly (or error) can impact a forecast using the full LIM. Figure 10 shows that \mathbf{p} ($\boldsymbol{\psi}_T$) PC1 skill is reduced by ignoring initial stratospheric (tropical heating) anomalies but is almost unaffected by ignoring initial tropical heating (stratospheric) anomalies, again as we might expect from the SVD results in Fig. 9. Ignoring initial heating anomalies degrades the PC2 skill for both variables, whereas ignoring initial stratospheric anomalies has no effect.

6. Tropical influences on stratospheric variability

Up to this point, we have treated the tropical and stratospheric influences as independent influences on extratropical tropospheric variability. In fact, as is implied by (3) and seen in Fig. 9a, tropical forcing also affects stratospheric variability. For example, approximately one third of the variance of ψ_S is due to the tropical portion of the linear operator. Also, ignoring initial \mathbf{H} anomalies in all forecasts reduces ψ_S PC2 forecast skill, by as much as 0.1 at longer than 25-day lead times. Interestingly, the initial \mathbf{H} anomaly associated with the maximum amplification of ψ_S /EOF2, shown in Fig. 11, is not particularly ENSO- or MJO-like. Such an initial \mathbf{H} anomaly can by itself produce a pronounced weakening of the stratospheric polar vortex, particularly over Hudson's Bay, in 21 days (top panel of Fig. 11).

If stratospheric anomalies can be forced by tropical heating, then some tropospheric impacts attributed to the stratosphere may be ultimately due to tropical heating. To investigate this possibility, a separate LIM operator $\tilde{\mathbf{L}}$ was constructed for ψ_T/ψ_S (i.e., by dropping \mathbf{H} from \mathbf{x}) and used to compute both $\tilde{\mathbf{C}}(\tau) = \exp(\tilde{\mathbf{L}}\tau)\mathbf{C}(0)$ and $\tilde{\mathbf{C}}_{\text{nos}}(\tau) = \exp(\tilde{\mathbf{L}}_{\text{nos}}\tau)\mathbf{C}(0)$. Removing stratospheric influences from *this* LIM (as in Fig. 5) had as large an impact on North Atlantic and polar \mathbf{p} lag-covariability as did the combined removal of tropical and stratospheric influences from the full LIM. This suggests that the actual stratospheric impact on the troposphere is overestimated when the LIM analysis does not also explicitly consider tropical heating.

How some tropical effects might falsely be attributed to the stratosphere is illustrated by examining tropical and stratospheric anomalies associated with optimal \mathbf{p} anomaly growth over long time intervals. For example, the full optimal initial condition for

amplification of \mathbf{p} /EOF1 over 35 days (not shown) is similar to that in Fig. 9b, but with greater \mathbf{H} and $\boldsymbol{\psi}_S$ amplitudes and lesser $\boldsymbol{\psi}_T$ and \mathbf{p} amplitudes. By day 35, it evolves into an AO-like SLP anomaly plus a pronounced stratospheric anomaly (that is, as $\exp(\mathbf{L}_{35})\mathbf{v}_1$, shown in the left panels of Fig. 12). If instead the same initial condition is allowed to evolve without any interactions with the tropical heating (that is, as $\exp(\mathbf{L}_{\text{noh}}35)\mathbf{v}_1$), the result, shown in the right panels of Fig. 12, is not only a much weaker \mathbf{p} anomaly but also a much weaker $\boldsymbol{\psi}_S$ anomaly. The tropical heating is thus largely responsible for the amplification of *both* surface and stratospheric anomalies in this case. Still, without stratospheric feedbacks (that is, using $\exp(\mathbf{L}_{\text{nos}}35)\mathbf{v}_1$, not shown) the amplified response is confined between 90°W and 90°E, suggesting that stratospheric feedbacks are responsible for the annular nature of the response in high latitudes. The importance of stratospheric feedback to \mathbf{p} anomalies over Siberia is also consistent with the pronounced surface temperature-stratospheric vortex relationship noted there by Thompson et al. (2002).

7. Potential deviations from linear behavior

It is gratifying that the LIM reproduces the observed 21-day lag-autocovariances over most of the northern hemisphere, as shown in section 3, despite inevitable errors associated with using real-world observations. In view of this overall success, the LIM's error in Fig. 3 over the area extending from the North Atlantic to the Barents Sea is notable. This discrepancy is more pronounced at the longer lags of 28 days and 35 days, as shown in Fig. 13. The LIM underestimates SLP persistence over the North Atlantic and overestimates it over the Barents Sea. Interestingly, this departure is limited to the surface: errors in $\boldsymbol{\psi}_{250}$ (upper panels in Fig. 13) and $\boldsymbol{\psi}_{750}$ (not shown) persistence are

small and statistically insignificant, both locally and in a "field significance" sense, even at the 90% level. (This was determined from 1000 Monte Carlo trials, in each of which the lag-autocovariance was computed from a dataset constructed by resampling the 35 winters with replacement). The surface error appears to have a coherent spatial structure, but it does not resemble any of the \mathbf{p} EOFs, and the variations of \mathbf{p} at the positive and negative error centers are almost exactly uncorrelated with each other.

One way for a LIM to fail is if its state vector \mathbf{x} is incomplete. One might suspect, for instance, that the underestimated persistence of tropical heating (see Fig. 3) is partly due to not explicitly including tropical sea surface temperatures (SST) in the model. Could this reduce the extratropical persistence as well? To address this question, a new LIM was constructed by extending the state vector with tropical SST components. Specifically, 7-day running mean anomalies of tropical skin temperatures \mathbf{S} from the NCEP reanalysis were projected onto their EOFs, and the PCs of the leading 15 EOFs (explaining about 70% of the weekly variance) were included in \mathbf{x} . This new model improved the 21-day forecast skill of heating throughout the Tropics, and to a lesser extent, also the Ψ_{250} forecast skill throughout the hemisphere. It also produced much-improved lag-covariances of tropical heating. Figure 14 shows the observed and predicted lag-autocorrelation functions of the leading PCs of each model variable. Note that by construction, they are identical at the 5-day training lag. Also shown are 90% confidence intervals estimated using the Monte Carlo procedure described above. Without \mathbf{S} in the LIM, the heating autocorrelation decays too rapidly with lag and soon lies outside the confidence interval.

Unfortunately, including \mathbf{S} in \mathbf{x} does not remove the problem in the SLP fields in Fig. 13. It does slightly improve North Pacific forecast skill, but not over the North Atlantic and Arctic regions, where the skill is actually slightly degraded. Also, although the persistence of \mathbf{p} PC1 is enhanced (Fig. 14), the oscillating component of the autocorrelation function (Ambaum and Hoskins 2002) is still not reproduced.

Two other variables, non-land skin temperature north of 60°N and column-integrated tropospheric diabatic heating north of 30°N , were also used in attempts to improve the LIM. Each was separately included in \mathbf{x} , retaining sufficient PCs to explain about 75% of the polar skin temperature and 59% of the extratropical heating weekly variances, but in both cases there was minimal impact on both forecast skill and the autocorrelation function.

The basic reason for our LIM's error in Fig. 13 may simply be that its assumptions are less valid over the North Atlantic. Since this is apparently a region of strong interaction between the surface and the stratosphere, any substantial seasonality in those interactions (associated with say the seasonality of tropopause heights) or in stratospheric variability (associated with, for example, the fact that stratospheric sudden warmings occur much more rarely in December; Charlton and Polvani (2007)) would invalidate the LIM's basic assumption of statistical stationarity. One indication of seasonality is that the correlation between the leading SLP and stratospheric PCs is .33 in January, but only .16 in December and .08 in February.

Nonlinear dynamical interactions in the North Atlantic may, of course, also decorrelate too slowly for any LIM to work. One might suspect this from the climatology of isentropic potential vorticity (PV) in the upper troposphere (see, for example, the

wintertime 330K PV surface in the NCEP/NCAR Reanalysis Atlas, <http://www.cdc.noaa.gov/cgi-bin/DataMenus.pl?dataset=NCEP>; Scott et al 1997). The PV gradient over the eastern Atlantic is weaker than the gradient over the eastern Pacific, indicative of stronger wave breaking and PV mixing that may occur too slowly to be approximated as white noise in a LIM constructed from weekly averages. Still, it is intriguing that Charlton et al. (2003) found only very weak nonlinear relationships between daily wintertime values of the AO at 1000 hPa and 70 hPa. Nonlinearity need not be only due to upper tropospheric wave breaking, of course. For example, distant ENSO forcing can produce subtly different responses over the North Pacific to warm versus cold ENSO events that are further amplified downstream over the North Atlantic (Sardeshmukh et al. 2000; Brönnimann 2007). Also, possibly asymmetric stratospheric responses to the warm vs. cold phases of ENSO (e.g., Taguchi and Hartmann 2006; Manzini et al. 2006; Wei et al. 2007) may result in asymmetric stratospheric feedbacks onto the polar SLP. Finally, our analysis has neglected nonlinear surface interactions, especially those involving high latitude sea ice and SST variations (e.g., Alexander et al. 2004; Deser et al. 2004), which would be particularly consistent with the regional confinement and shallowness of the LIM's persistence error.

8. Summary and Concluding Remarks

It is a truism that correlation does not imply causation, and mere documentations of correlations and lag-correlations do not establish dynamical relationships between a system's variables. Linear inverse modeling goes beyond this by estimating from observations an effectively linear dynamical feedback matrix \mathbf{L} encapsulating the dynamical relationships. Its key assumption is that the system's lag-covariance matrices at different lags are linked as $\mathbf{C}(\tau) = \exp(\mathbf{L}\tau) \mathbf{C}(0)$. It uses this relationship to estimate \mathbf{L}

from one lag, and then tests it at other lags (this is the “Tau test” of Penland and Sardeshmukh 1995). Successful passage of the Tau test justifies extensive dynamical diagnosis of the system through investigation of the structure and properties of \mathbf{L} , as done here. The Tau test can fail if one has not included all dynamically active agents in the analysis, if the statistics are not stationary, or if the dynamics are not even *effectively* linear (i.e if the nonlinear interactions cannot be approximated as linear terms plus stochastic noise). Dynamical diagnosis of a system from observed linear correlations is therefore either importantly incomplete (even if the dynamics are effectively linear) or inadequate if the Tau test fails.

In this study our focus was on elucidating the relative impacts of tropical diabatic heating and stratospheric circulation anomalies on the extratropical tropospheric circulation anomalies in winter. To this end we constructed a LIM from the zero-lag and 5-day lag covariances of the observed 7-day running mean anomalies. To justify our linear diagnosis, we performed the “Tau test”, and successfully demonstrated the LIM’s ability to reproduce the observed lag-covariance statistics at other lags than the lag on which the LIM was trained. We then analyzed interactions among the LIM’s variables by shutting off some of them in the LIM’s \mathbf{L} operator, and also by examining the forecast impacts of setting some components of the initial conditions to zero. Our demonstration that the dynamics of weekly averages are effectively linear and stochastically driven also enabled a second-order closure of the moment equations, in particular a meaningful discussion of the streamfunction variance budget. It additionally justified a meaningful singular vector analysis of the system’s propagator $\exp(\mathbf{L}\tau)$, which shed further light on the tropical and stratospheric influences on extratropical tropospheric circulation variability and predictability.

As a result of this diagnosis, we conclude that tropical diabatic heating greatly enhances persistent variability over most of the northern hemisphere, especially over the Pacific and North America, whereas stratospheric effects are largely confined to the polar region. Over the North Atlantic, both effects are important, although our results also suggest that some indirect tropical effects could be mistaken for direct stratospheric influences. Even in the absence of these “external” tropical and stratospheric influences, however, some persistent variability remains that can be linked to the leading eigenmodes of the LIM’s internal extratropical tropospheric evolution operator. The two eigenmodes associated with north-south dipole variations across the North Atlantic jet represent the implicit inclusion in \mathbf{L} of linear synoptic-eddy feedbacks on the slowly varying circulation (e.g., Gerber and Vallis 2007). The eigenmode with a circumglobal zonal wavenumber-5 structure is suggestive of a quasi-stationary barotropic mode in the Pacific waveguide (Branstator 2002) and enhances persistence near the dateline. None of the leading eigenmodes of the internal operator, however, are eigenmodes of the full operator, raising the possibility that coupling to the tropics and stratosphere does not merely act to select some extratropical modes over others but also modifies the modes themselves.

In general, we find that tropically forced anomalies extend through the depth of the troposphere and into the stratosphere, whereas stratospherically generated anomalies tend to be largest at the surface and relatively weak at mid-tropospheric levels. The relative confinement of the stratospheric influence to the North Atlantic and Arctic is consistent with the view that it is associated with large PV anomalies at and above the tropopause (e.g., Ambaum and Hoskins 2002). These anomalies have a surface footprint induced by balanced PV dynamics that is relatively large when the tropopause is closer to the surface, near Scandinavia, Greenland, and Siberia. The mid-tropospheric variability

driven by tropical heating is associated with weaker PV anomalies, and a correspondingly smaller surface impact.

As a related consequence, our results suggest that while the classic NAO -- with opposing centers of action over Iceland and the Azores -- is a largely tropospheric phenomenon driven by synoptic-eddy feedbacks and to a lesser extent tropical heating, the stratospheric anomalies generated by the NAO then feed back on the remainder of the polar region, producing the more zonally symmetric AO pattern associated with **p**/EOF1. [Kodera and Kuroda (2004) made a somewhat similar distinction.] One might therefore expect studies that are based upon the time series of a single NAO or AO pattern to have difficulty distinguishing stratospheric from tropical effects.

Past studies considering relationships between the tropics and the extratropical stratosphere have typically focused on ENSO-related tropical SST forcing. WNS emphasized the somewhat obvious point that ultimately the extratropical response to tropical forcing depends on the evolving tropical heating anomalies and not the SST anomalies themselves. In our study, too, the heating pattern contributing to the greatest possible stratospheric anomaly amplification over a month is similar but not identical to the canonical ENSO heating anomaly pattern (for example, cf. Figs. 1 and 11), and there are also important differences between these and the initial heating pattern associated with the greatest impact over the Atlantic.

Finally, although our focus here was on tropical and stratospheric influences on extratropical tropospheric variability, our LIM also allows investigations of influences in the reverse direction, which we did not pursue here. The influence on tropical heating in particular is relatively unexplored territory. Sardeshmukh and Sura (2007) recently

showed a strong impact of low-frequency extratropical anomalies on the thermal structure of the tropical troposphere on longer time scales. To what extent this impacts tropical heating variability is an intriguing question.

Acknowledgements

The authors thank Judith Perlwitz and Cécile Penland for useful conversations, and three anonymous reviewers for helpful comments on an earlier version of this paper. This work was partially supported by a grant from NOAA CLIVAR-Pacific.

References

- Alexander, M. A., U. S. Bhatt, J. E. Walsh, M. S. Timlin, J. S. Miller, and J. D. Scott, 2004: The atmospheric response to realistic arctic sea ice anomalies in an AGCM during winter. *J. Climate*, **17**, 890-905.
- Ambaum, M. H. P. and B. J. Hoskins, 2002: The NAO Troposphere-Stratosphere connection. *J. Climate*, **15**, 1969-1978.
- Ambaum, M. H. P., B. J. Hoskins, and D. B. Stephenson, 2001: Arctic oscillation or North Atlantic oscillation? *J. Climate*, **14**, 3495-3507.
- Bader, J. and M. Latif, 2005: North Atlantic Oscillation response to anomalous Indian Ocean SST in a coupled GCM. *J. Climate*, **18**, 5382-5389.
- Baldwin, M. P., and T. J. Dunkerton, 2001: Stratospheric harbingers of anomalous weather regimes. *Science*, **294**, 581-584.
- Baldwin, M. P., D. B. Stephenson, D. W. J. Thompson, T. J. Dunkerton, A. J. Charlton, and A. O'Neill, 2003: Stratospheric memory and skill of extended-range weather forecasts. *Science*, **301**, 636-640.
- Borges, M. D., and P. D. Sardeshmukh, 1995: Barotropic Rossby wave dynamics of zonally varying upper level flows during northern winter. *J. Atmos. Sci.*, **52**, 3779-3796.
- Branstator, G. W., 1995: Organization of storm track anomalies by recurring low-frequency circulation anomalies. *J. Atmos. Sci.*, **52**, 207-226.

- Branstator, G. W., 2002: Circumglobal teleconnections, the jet stream waveguide, and the North Atlantic oscillation. *J. Climate*, **15**, 1893-1910.
- Branstator, G. W., and J. Frederikson, 2003: The seasonal cycle of interannual variability and the dynamical imprint of the seasonally varying mean state. *J. Atmos. Sci.*, **60**, 1577–1592.
- Brönnimann, S., 2007: Impact of El Niño-Southern Oscillation on European climate. *Rev. Geophys.*, **45**, RG3003, doi:10.1029/2006RG000199.
- Cai, M., and H. M. van den Dool, 1991: Low-frequency waves and traveling storm tracks. Part I: Barotropic component. *J. Atmos. Sci.*, **48**, 1420-1436.
- Camp, C. D., and K. K. Tung, 2007: Stratospheric polar warming by ENSO in winter: A statistical study. *Geophys. Res. Lett.*, **34**, doi:10.1029/2006GL028521.
- Charlton, A. J., A. O'Neill, D. B. Stephenson, W. A. Lahoz, and M. P. Baldwin, 2003: Can knowledge of the state of the stratosphere be used to improve statistical forecasts of the troposphere? *Q. J. R. Meteorol. Soc.*, **129**, 3205-3224.
- Charlton, A. J., and L. M. Polvani, 2007: A new look at stratospheric sudden warmings. Part I: Climatology and modeling benchmarks. *J. Climate*, **20**, 449-469.
- Christiansen, B., 2005: Downward propagation and statistical forecast of the near-surface weather. *J. Geophys. Res.*, **110**, D14104, doi:10.1029/2004JD005431.
- Corti, S., F. Molteni, and T. N. Palmer, 1999: Signature of recent climate change in frequencies of natural atmospheric circulation regimes. *Nature*, **29**, 799-802.

- Deser, C., 2000: On the teleconnectivity of the “Arctic Oscillation.” *Geophys. Res. Lett.*, **27**, 779-782.
- Deser, C., G. Magnusdottir, R. Saravana, and A. Phillips, 2004: The effect of North Atlantic SST and sea ice anomalies on the winter circulation in CCM3. Part II: Direct and indirect components of the response. *J. Climate*, **17**, 877-889.
- Egger, J., and H.-D. Schilling, 1983: On the theory of the long-term variability of the atmosphere. *J. Atmos. Sci.*, **40**, 1073-1085.
- Farrell, B., 1988: Optimal excitation of neutral Rossby waves. *J. Atmos. Sci.*, **45**, 163-172.
- Feldstein, S. B., 2000: The timescale, power spectra, and climate noise properties of teleconnection patterns. *J. Climate*, **13**, 4430.
- Gerber, E. P., and G. K. Vallis, 2007: Eddy-zonal flow interactions and the persistence of the zonal index. *J. Atmos. Sci.*, in press.
- Hasselmann, K., 1976: Stochastic climate models. Part I. Theory. *Tellus*, **28**, 474-485.
- Hoerling M. P., J. W. Hurrell, and T. Y. Xu, 2001: Tropical origins for recent North Atlantic climate change. *Science*, **292**, 90-92.
- Holton, J. R., and H. C. Tan, 1982: The quasi-biennial oscillation in the Northern Hemisphere lower stratosphere. *J. Meteorol. Soc. Jpn.*, **60**, 140-148.
- Hoskins, B. J., and D. J. Karoly, 1981: The steady linear response of a spherical atmosphere to thermal and orographic forcing. *J. Atmos. Sci.*, **38**, 1179-1196.

- Hoskins, B. J. and T. Ambrizzi, 1993: Rossby wave propagation on a realistic longitudinally varying flow. *J. Atmos. Sci.*, **50**, 1661-1671.
- Kimoto, M., and M. Ghil, 1993: Multiple flow regimes in the Northern Hemisphere winter. Part I: Methodology and hemispheric regimes. *J. Atmos. Sci.*, **50**, 2625-2643.
- Kodera, K., and Y. Kuroda, 2004: Two teleconnection patterns involved in the North Atlantic/Arctic Oscillation. *Geophys. Res. Lett.*, **31**, L20201, doi:10.1029/2004GL020933.
- Kushnir, Y. and J. M. Wallace, 1989: Low-frequency variability in the Northern Hemisphere Winter - Geographical-distribution, structure and time-scale dependence. *J. Atmos. Sci.*, **46**, 3122-3142.
- Lahoz, W. A., 2000: Northern Hemisphere winter stratospheric variability in the Met. Office Unified Model. *Quart. J. Roy. Meteor. Soc.*, **126**, 2605–2630.
- Lau, N.-C., 1988: Variability of the observed midlatitude storm tracks in relation to low-frequency changes in the circulation pattern. *J. Atmos. Sci.*, **45**, 2718-2743.
- Lin, H., J. Derome, R. J. Greatbatch, K. A. Peterson, and J. Lu, 2002: Tropical links of the Arctic oscillation. *Geophys. Res. Lett.*, **29**, 1943-1946.
- Manzini, E., M. A. Giorretta, M. Esch, L. Kornblueh, and E. Roeckner, 2006: The influence of sea surface temperatures on the northern winter stratosphere: Ensemble simulations with the MAECHAM5 model. *J. Climate*, **19**, 3863-3881.

- Mitas, C. M., and W. A. Robinson, 2005: Atmospheric stability in a generalized barotropic model. *J. Atmos. Sci.*, **62**, 476-491.
- Newman, M., P. D. Sardeshmukh, and C. Penland, 1997: Stochastic forcing of the wintertime extratropical flow. *J. Atmos. Sci.*, **54**, 435—455.
- Newman, M., M. A. Alexander, C. R. Winkler, J. D. Scott, and J. J. Barsugli, 2000: A linear diagnosis of the coupled extratropical Ocean-Atmosphere system in the GFDL GCM. *Atmospheric Sciences Letters*, **1**, 14-25.
- Newman, M., P. D. Sardeshmukh, C. R. Winkler, and J. S. Whitaker, 2003: A study of subseasonal predictability. *Mon. Wea. Rev.*, **131**, 1715-1732.
- Papanicolaou, G. and W. Kohler, 1974: Asymptotic theory of mixing stochastic ordinary differential equations. *Commun. Pure Appl. Math.*, **27**, 641-668.
- Penland, C., 1996: A stochastic model of IndoPacific sea surface temperature anomalies. *Physica D*, **98**, 534--558.
- Penland, C., and M. Ghil, 1993: Forecasting Northern Hemisphere 700-mb geopotential heights using principal oscillation patterns. *Mon. Wea. Rev.*, **121**, 2355–2372.
- Penland, C., and L. Matrosova, 1994: A balance condition for stochastic numerical models with application to the El Niño-Southern Oscillation. *J. Climate*, **7**, 1352-1372.
- Penland, C., and P. D. Sardeshmukh, 1995: The optimal growth of tropical sea surface temperature anomalies. *J. Climate*, **8**, 1999—2024.

- Randel, W. J., F. Wu, R. Swinbank, J. Nash, and A. O'Neill, 1999: Global QBO circulation derived from UKMO stratospheric analyses. *J. Atmos. Sci.*, **56**, 457-474.
- Sardeshmukh, P. D., and B. J. Hoskins, 1984: Spatial smoothing on the sphere. *Mon. Wea. Rev.*, **112**, 2524—2529.
- Sardeshmukh, P. D., and B. J. Hoskins, 1988: The generation of global rotational flow by steady idealized divergence. *J. Atmos. Sci.*, **45**, 1228-1251.
- Sardeshmukh, P. D., 1993: The baroclinic chi problem and its application to the diagnosis of atmospheric heating rates. *J. Atmos. Sci.*, **50**, 1099—1112.
- Sardeshmukh, P. D., M. Newman, and M. D. Borges, 1997: Free barotropic Rossby wave dynamics of the wintertime low-frequency flow. *J. Atmos. Sci.*, **54**, 5—23.
- Sardeshmukh, P. D., M. Newman, and C. R. Winkler, 1999: Dynamically consistent estimates of diabatic heating. Proceedings, 24th Annual Climate Diagnostics and Prediction Workshop, Tucson, AZ, 172--175.
- Sardeshmukh, P. D., G. P. Compo, and C. Penland, 2000: Changes of probability associated with El Niño. *J. Climate*, **13**, 4268-4286.
- Sardeshmukh, P. D., and P. Sura, 2007: Multi-scale impacts of variable heating in climate. *J. Climate*, **20**, 5677-5695.
- Scott, J. D., M. A. Alexander, J. A. Collins, and C. A. Smith, 1997: Interactive visualization of climate data on the WWW. *Bull. Amer. Met. Soc.*, **78**, 1985-1989.

- Simmons, A. J., 1982: The forcing of stationary wave motion by tropical diabatic heating. *Quart. J. Roy. Meteor. Soc.*, **108**, 503—534.
- Simmons, A. J., J. M. Wallace, and G. W. Branstator, 1983: Barotropic wave propagation and instability, and atmospheric teleconnection patterns. *J. Atmos. Sci.*, **40**, 1363—1392.
- Taguchi and D. L. Hartmann, 2006: Increased occurrence of stratospheric sudden warmings during El Niño as simulated by WACCM. *J. Climate*, **19**, 324-332.
- Thompson, D. W. J., and J. M. Wallace, 2000: Annular modes in the extratropical circulation. Part I. Month-to-month variability. *J. Climate*, **13**, 1000-1016.
- Thompson, D. W. J., M. P. Baldwin, and J. M. Wallace, 2002: Stratospheric connection to Northern Hemisphere wintertime weather: Implications for prediction. *J. Climate*, **15**, 1421-1428.
- Thompson, D. W. J., J. C. Furtado, and T. G. Shepherd, 2006: On the tropospheric response to anomalous stratospheric wave drag and radiative heating. *J. Atmos. Sci.*, **63**, 2616-2629.
- Valdes, P. J., and B. J. Hoskins, 1989: Linear stationary wave simulations of the time-mean climatological flow. *J. Atmos. Sci.*, **46**, 2509-2527.
- Wei, K., W. Chen, and R. Huang, 2007: Association of tropical Pacific sea surface temperatures with the stratospheric Holton-Tan oscillation in the Northern Hemisphere winter. *Geophys. Res. Lett.*, **34**, doi:10.1029/2007GL030478.

- Whitaker, J. S., and P. D. Sardeshmukh, 1998: A linear theory of extratropical synoptic eddy statistics. *J. Atmos. Sci.*, **55**, 237-258.
- Winkler, C. R., M. Newman, and P. D. Sardeshmukh, 2001: A linear model of wintertime low-frequency variability. Part I: Formulation and forecast skill. *J. Climate*, **14**, 4474-4494.
- Zhou, S., and A. J. Miller, 2005: The interaction of the Madden-Julian oscillation and the Arctic oscillation. *J. Climate*, **18**, 143-159.

9. Figures

Figure 1: Leading EOFs of selected variables used in the model. Top row: 30 hPa streamfunction (ψ_{30}), 2nd row: 250 hPa streamfunction (ψ_{250}), 3rd row: slp (p), bottom row: tropical heating (H). Contour intervals are arbitrary, but the same for EOFs 1 and 2. The overall sign of each panel is also arbitrary. Within each panel, one sign is gray shading and thick contours, and the other sign is thin contours. Zero contours in this and all subsequent figures (except Fig. 2) are removed for clarity.

Figure 2. Skill of 21-day forecasts for the “full” LIM (b and d), the tropospheric streamfunction/tropical heating, or “ ψ_T/H ,” LIM (a), and the SLP/stratospheric streamfunction, or “ p/ψ_S ,” LIM (c). a) and b): ψ_{250} skill; c) and d): p skill. Contour interval is 0.1; the zero contour is dashed.

Figure 3. Observed (left panels) and LIM-predicted (right panels) 21-day lag-covariance. Top panels: 250 hPa streamfunction (ψ_{250}) (contour/shading interval = $10^{13} \text{ m}^4 \text{ s}^{-2}$). Middle panels: slp (p) (contour/shading interval = 50000 Pa^2). Bottom panels: diabatic heating (H) (contour/shading interval = $0.1 \text{ Pa}^2 \text{ K}^2 \text{ s}^{-2}$). Orange/red shading represents positive values, and blue shading represents negative values.

Figure 4. Variance of 250 hPa streamfunction (ψ_{250}) for 7-day running means (left panels) and 21-day running means (right panels). Top) Observed, middle) from LIM, bottom) from LIM with the “forcing” terms (heating and stratosphere) removed. Contour interval is $4.5 \times 10^{13} \text{ m}^4 \text{ s}^{-2}$ in the left panels and $3 \times 10^{13} \text{ m}^4 \text{ s}^{-2}$ in the right panels.

Figure 5. Comparison of the effects of tropical heating (**H**) and stratospheric streamfunction (ψ_s) upon 21-day lag-covariance. Left panels show 250 hPa streamfunction (ψ_{250}) lag-covariance and right panels show SLP (**p**) lag-covariance; contour interval and shading are the same as in Fig. 3.

Figure 6. 250 hPa streamfunction (ψ_{250}) portion of the three leading eigenmodes of \mathbf{L}_{TT} . (a) Least damped eigenmode. (b) Second eigenmode. (c) Third eigenmode, most energetic phase. Contour interval is arbitrary. The overall sign of each panel is also arbitrary; within each panel, values of one sign are depicted with gray shading and thick contours, and the other sign with thin contours.

Figure 7. The local variance budget for 250 hPa streamfunction (see text for description of terms). Note that the sum of the panels within the green shaded region is zero, and the panel in the upper left corner is equal to the sum of the panels in the white shaded region. Contour and shading interval is $6 \times 10^{12} \text{ m}^4 \text{ s}^{-2} \text{ da}^{-1}$; positive values are shaded in yellow/red tones and negative in blue.

Figure 8. Comparison of Maximum Amplification (MA) curves, defined as $[\lambda_1(\tau)]^2$ determined by the SVD of $\mathbf{G}(\tau)$ under the L2 norm of **p**, ψ_T , **H**, and ψ_s , respectively.

Figure 9. (Column a) Day 21 response to the tropical portion (30 S-30 N) of the optimal initial condition for maximizing the amplitude of ψ_T /EOF1. (Column b) Day 21 response to the extratropical portion (35N-90N) of the optimal initial condition for maximizing the amplitude of **p**/EOF1. The full optimal initial condition in both cases is normalized to unity. Contour intervals: Top row: 30 hPa streamfunction (ψ_{30} ; $3.75 \times 10^5 \text{ m}^2 \text{ s}^{-1}$). Middle row: 250 hPa streamfunction (ψ_{250} ; $2.5 \times 10^5 \text{ m}^2 \text{ s}^{-1}$). Bottom row: SLP (**p**; 20 Pa).

Positive values are indicated by shading and thick contours, and negative values by thin contours.

Figure 10. Forecast skill of leading SLP and tropospheric streamfunction PCs (blue lines), compared to skill obtained when either tropical heating (red lines) or stratospheric streamfunction (green lines) initial conditions are removed. All forecast skill is cross-validated. Note that the same linear operator is used to generate all three sets of forecasts. Top: skill for the two leading tropospheric streamfunction (ψ_T) PCs. Bottom: skill for the two leading SLP (p) PCs. In both panels, solid lines indicate PC 1 skill and dashed lines indicate PC 2 skill.

Figure 11. Day 21 30 hPa streamfunction response of the full LIM (top) to the initial tropical heating anomaly shown in the bottom panel. This heating pattern is taken from the optimal initial condition leading to maximum amplification of ψ_s /EOF2 over 21 days. Contour intervals are Top: $3.75 \times 10^5 \text{ m}^2\text{s}^{-1}$ and Bottom: $7.5 \times 10^{-3} \text{ PaKs}^{-1}$. Positive values are indicated by shading and thick contours, and negative values by thin contours.

Figure 12. Day 35 p (top) and ψ_{30} (bottom) response to the leading singular vector for a 35 day lag, where the norm is the amplification of the leading p EOF. Left panels show anomalies evolved using the full LIM. Right panels show anomalies evolved without tropical influences; that is, evolved by L_{noh} . Contour intervals are 10 Pa for the top row and $3.75 \times 10^5 \text{ m}^2\text{s}^{-1}$ for the bottom row. Positive values are indicated by shading and thick contours, and negative values by thin contours.

Figure 13. Difference between observed and LIM-predicted 28-day (left) and 35-day (right) lag-covariances, for ψ_{250} (top panels) and p (bottom panels). Positive values are

indicated by thick contours and negative values by thin contours. Contour intervals are as in Fig 3. Gray shading indicates where the LIM lag-covariance does not lie within the 90% confidence interval for the observed lag-covariance, based on a Monte Carlo test; see text for more details.

Figure 14. Comparison of the autocorrelation function of the leading principal component of each model variable, for observations (solid line) and the LIM (dashed line). Gray shading indicates the 90% confidence interval for the observed autocorrelation, based on a Monte Carlo test. Results obtained using an extended LIM with additional tropical oceanic skin temperature components are shown as dashed-dotted lines.

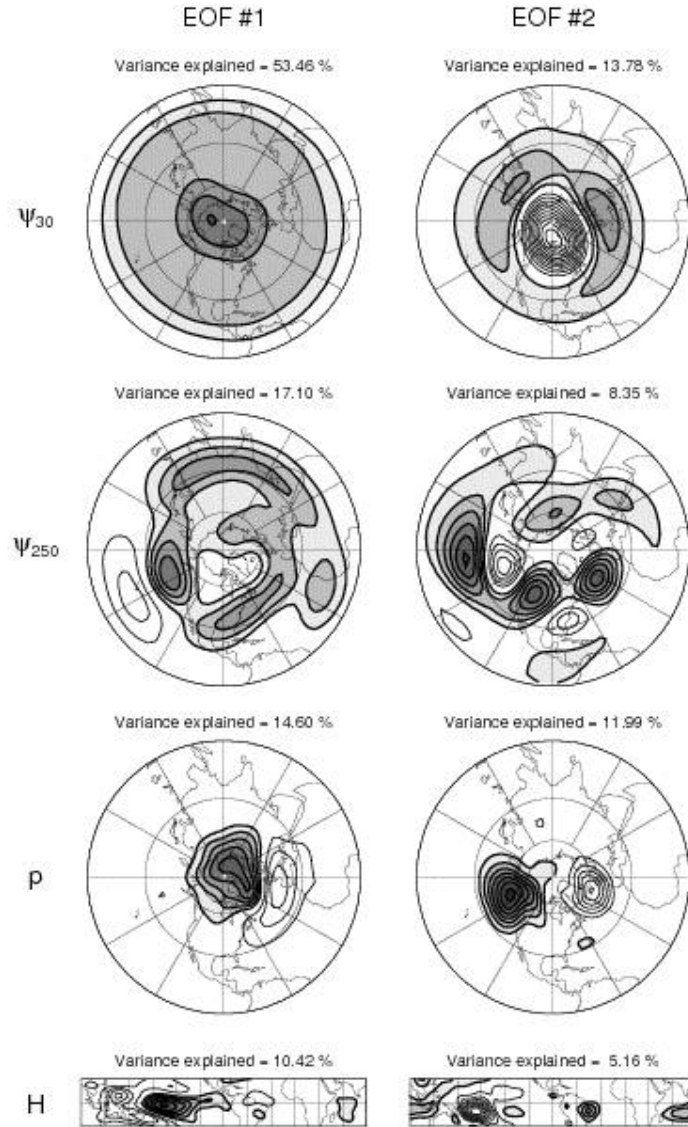


Figure 1: Leading EOFs of selected variables used in the model. Top row: 30 hPa streamfunction (ψ_{30}), 2nd row: 250 hPa streamfunction (ψ_{250}), 3rd row: slp (p), bottom row: tropical heating (H). Contour intervals are arbitrary, but the same for EOFs 1 and 2. The overall sign of each panel is also arbitrary. Within each panel, one sign is gray shading and thick contours, and the other sign is thin contours. Zero contours in this and all subsequent figures (except Fig. 2) are removed for clarity.

Anomaly correlation skill of Day 21 forecasts

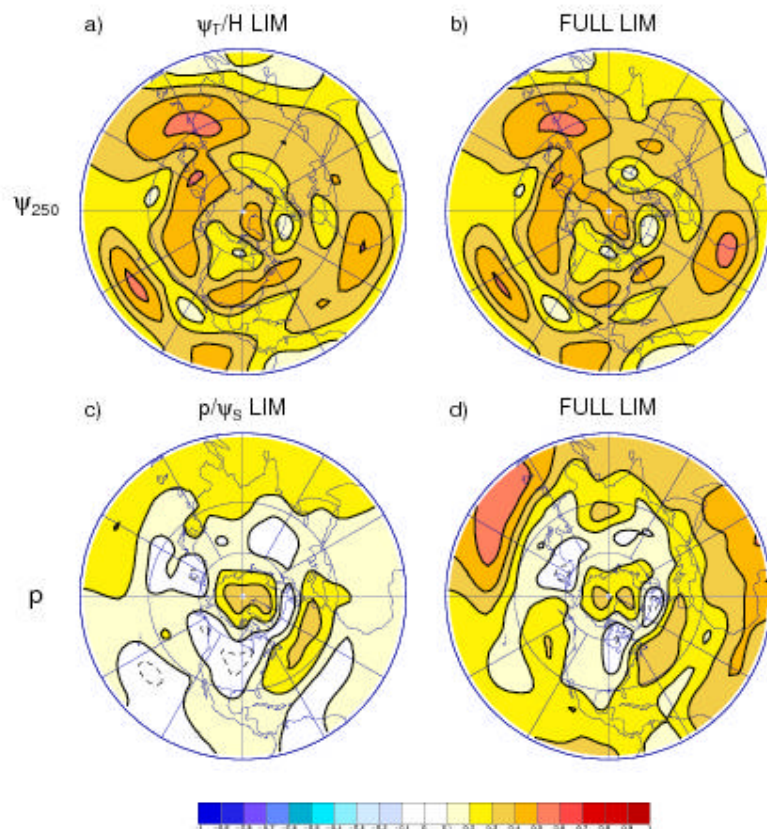


Figure 2. Skill of 21-day forecasts for the “full” LIM (b and d), the tropospheric streamfunction/tropical heating, or “ ψ_T/H ,” LIM (a), and the SLP/stratospheric streamfunction, or “ p/ψ_S ,” LIM (c). a) and b): ψ_{250} skill; c) and d): p skill. Contour interval is 0.1; the zero contour is dashed.

Observed and predicted 21-day lag-covariances

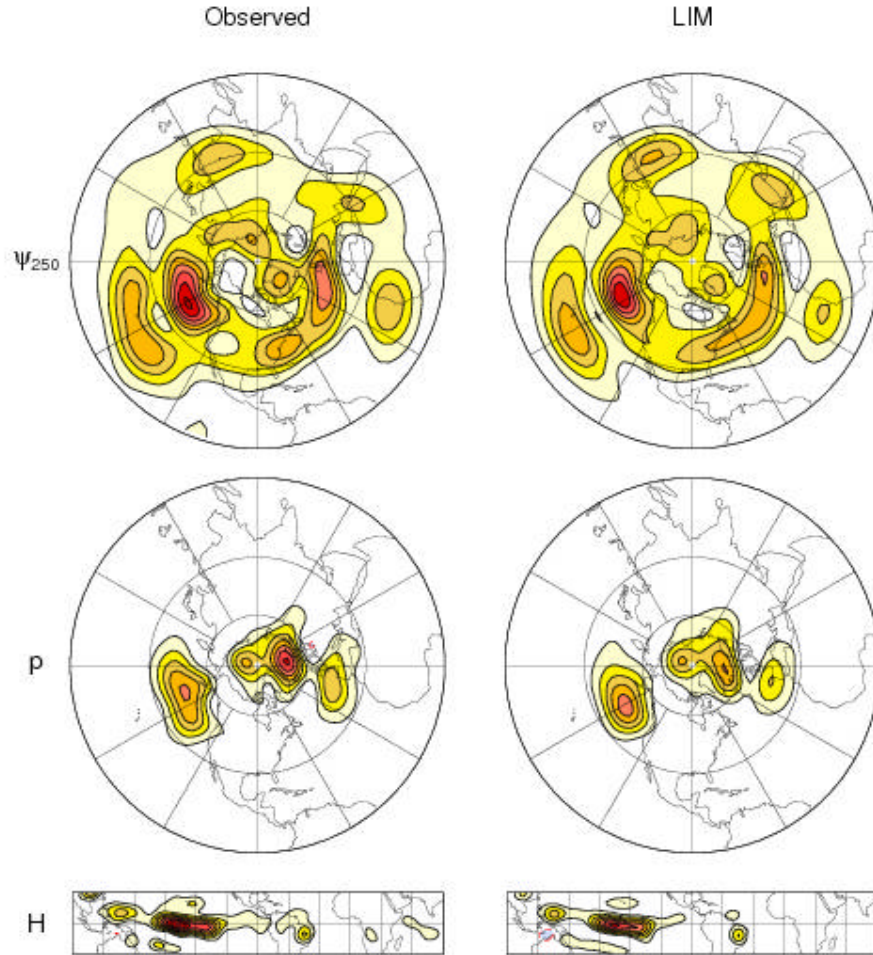


Figure 3. Observed (left panels) and LIM-predicted (right panels) 21-day lag-covariance. Top panels: 250 hPa streamfunction (Ψ_{250}) (contour/shading interval = $10^{13} \text{ m}^4 \text{ s}^{-2}$). Middle panels: slp (p) (contour/shading interval = 50000 Pa^2). Bottom panels: diabatic heating (H) (contour/shading interval = $0.1 \text{ Pa}^2 \text{ K}^2 \text{ s}^{-2}$). Orange/red shading represents positive values, and blue shading represents negative values.

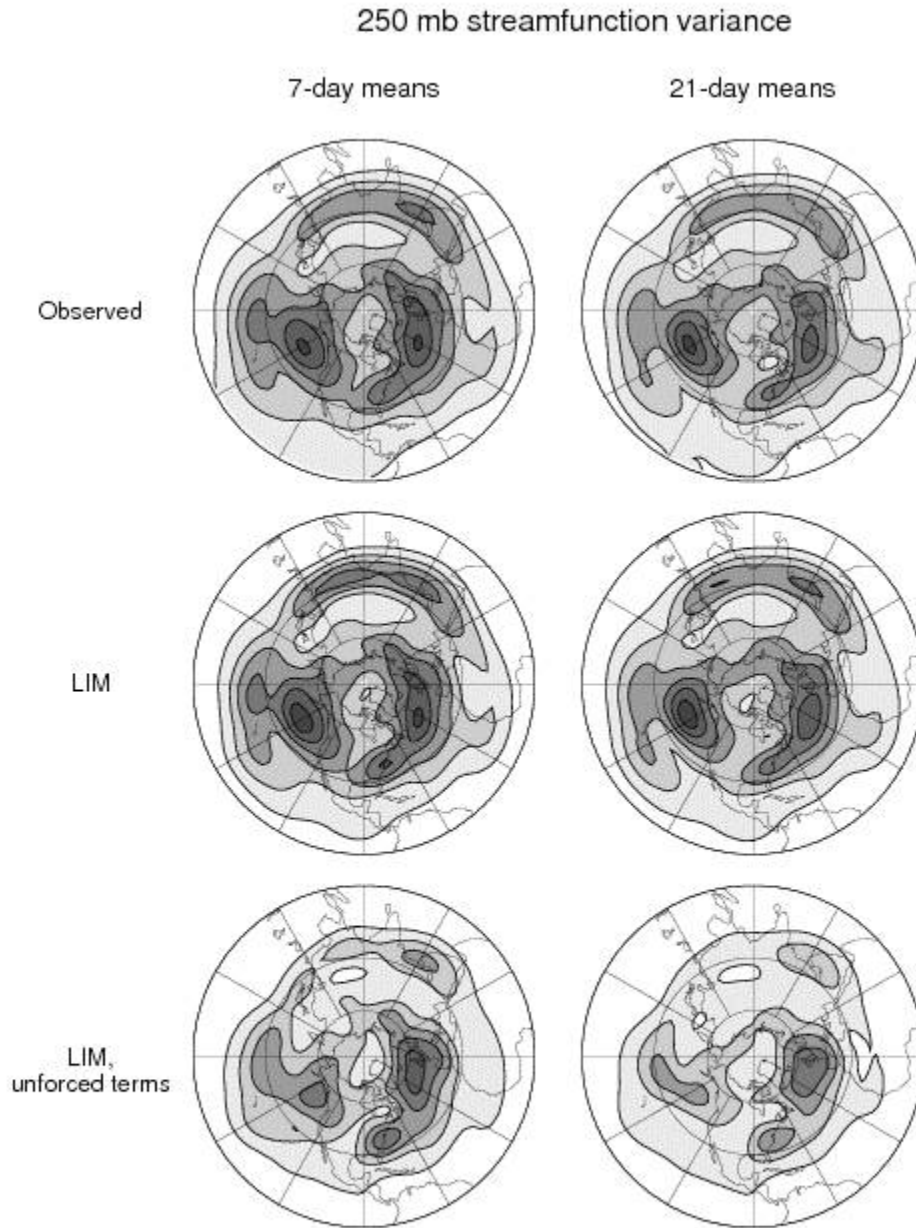


Figure 4. Variance of 250 hPa streamfunction (ψ_{250}) for 7-day running means (left panels) and 21-day running means (right panels). Top) Observed, middle) from LIM, bottom) from LIM with the “forcing” terms (heating and stratosphere) removed. Contour interval is $4.5 \times 10^{13} \text{ m}^4 \text{ s}^{-2}$ in the left panels and $3 \times 10^{13} \text{ m}^4 \text{ s}^{-2}$ in the right panels.

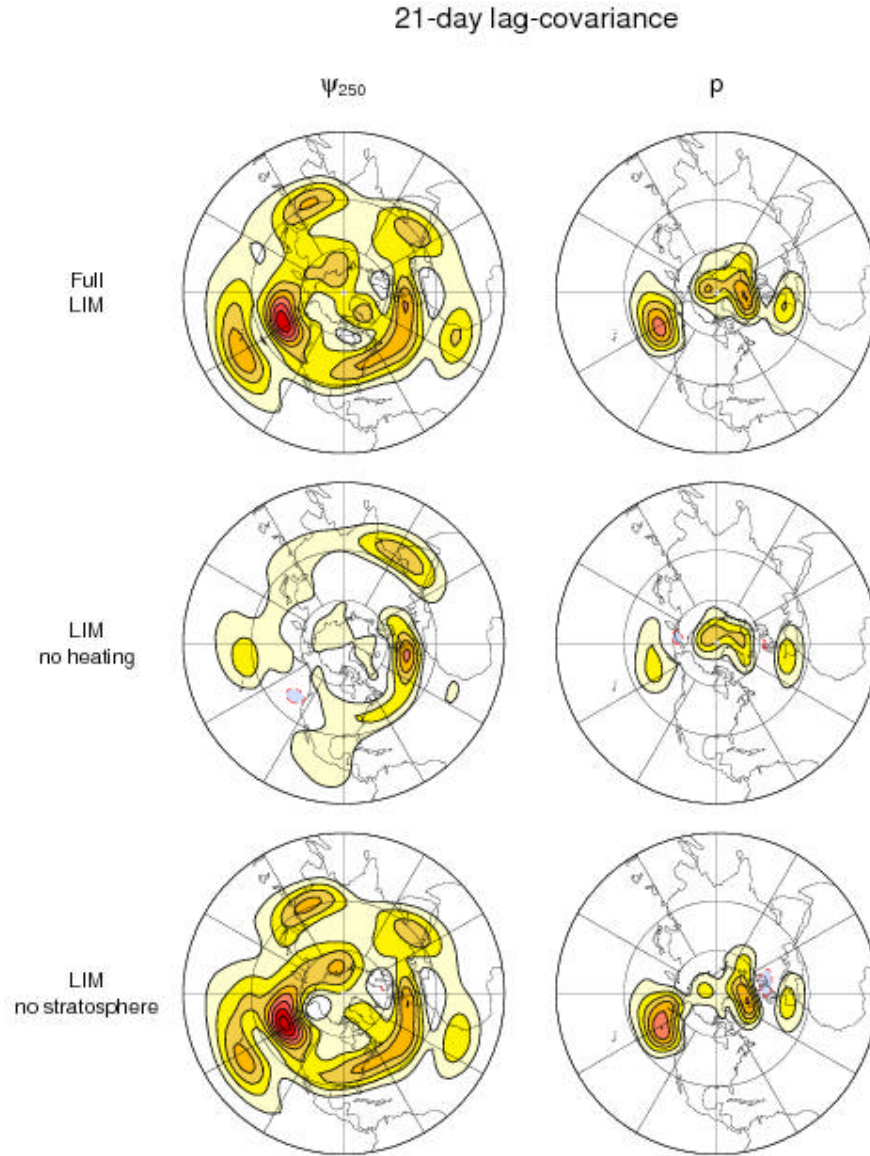


Figure 5. Comparison of the effects of tropical heating (**H**) and stratospheric streamfunction (Ψ_s) upon 21-day lag-covariance. Left panels show 250 hPa streamfunction (Ψ_{250}) lag-covariance and right panels show SLP (p) lag-covariance; contour interval and shading are the same as in Fig. 3.

Leading eigenmodes of the
internal tropospheric dynamical operator

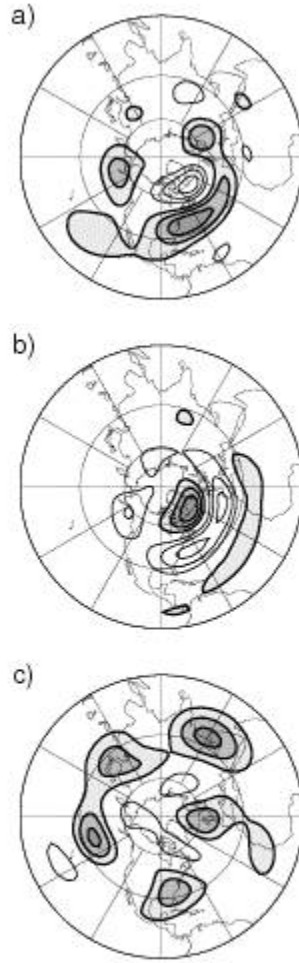


Figure 6. 250 hPa streamfunction (ψ_{250}) portion of the three leading eigenmodes of \mathbf{L}_{TT} . (a) Least damped eigenmode. (b) Second eigenmode. (c) Third eigenmode, most energetic phase. Contour interval is arbitrary. The overall sign of each panel is also arbitrary; within each panel, values of one sign are depicted with gray shading and thick contours, and the other sign with thin contours.

250 hPa streamfunction variance budget

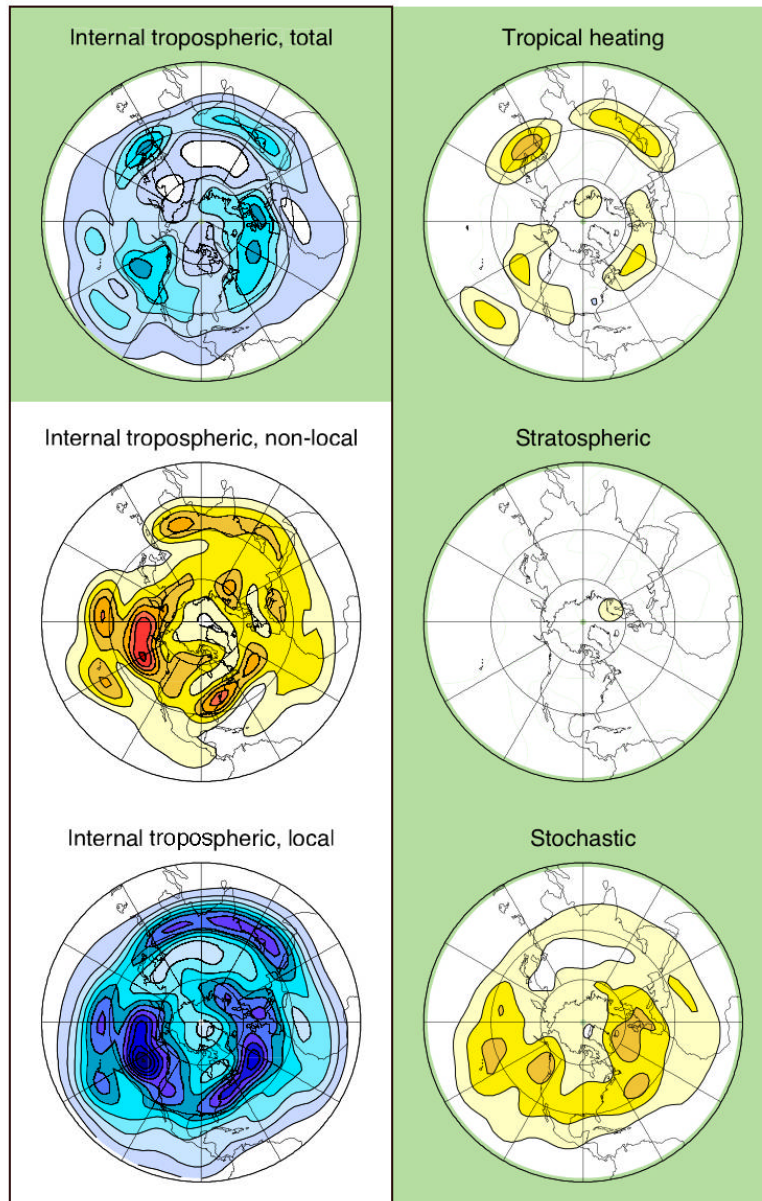


Figure 7. The local variance budget for 250 hPa streamfunction (see text for description of terms). Note that the sum of the panels within the green shaded region is zero, and the panel in the upper left corner is equal to the sum of the panels in the white shaded region. Contour and shading interval is $6 \times 10^{12} \text{ m}^4 \text{ s}^{-2} \text{ da}^{-1}$; positive values are shaded in yellow/red tones and negative in blue.

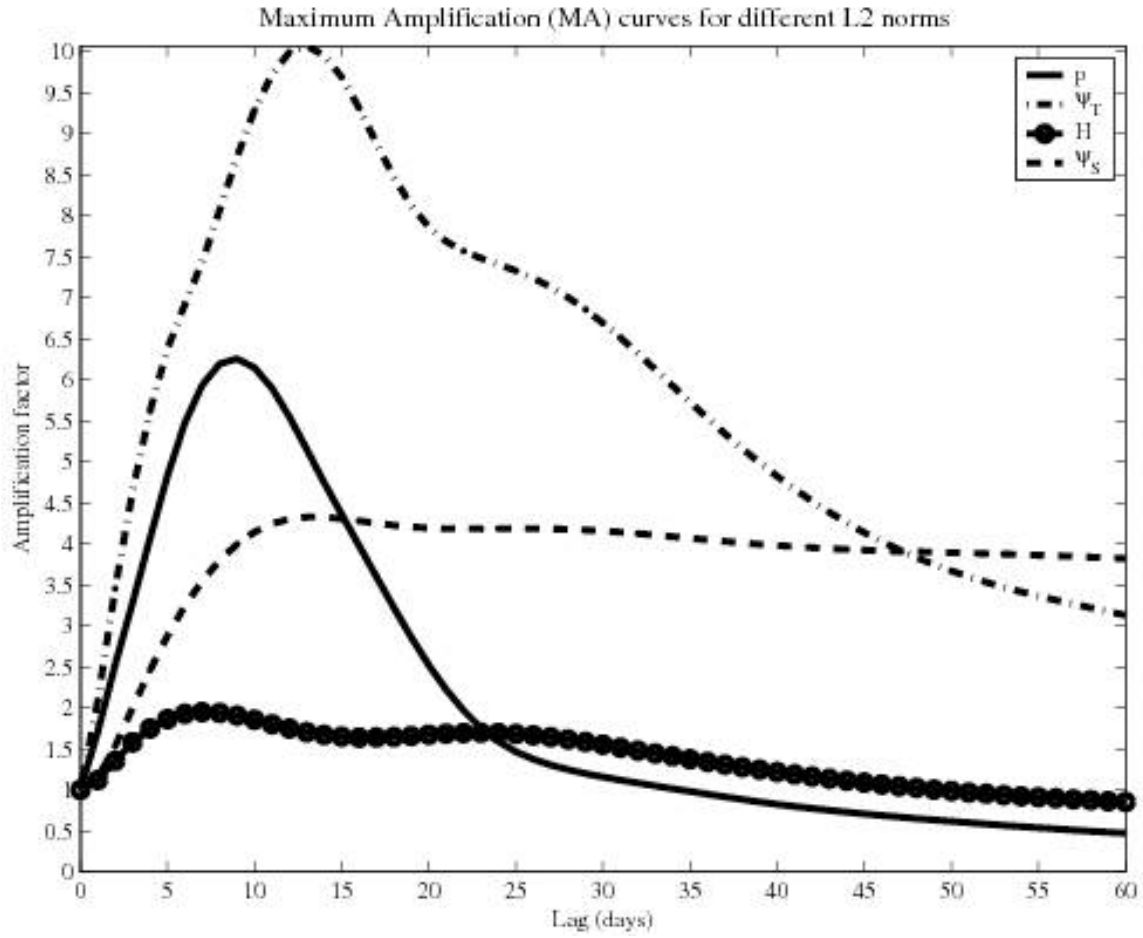


Figure 8. Comparison of Maximum Amplification (MA) curves, defined as $[\lambda_1(\tau)]^2$ determined by the SVD of $\mathbf{G}(\tau)$ under the L2 norm of \mathbf{p} , ψ_T , \mathbf{H} , and ψ_S , respectively.

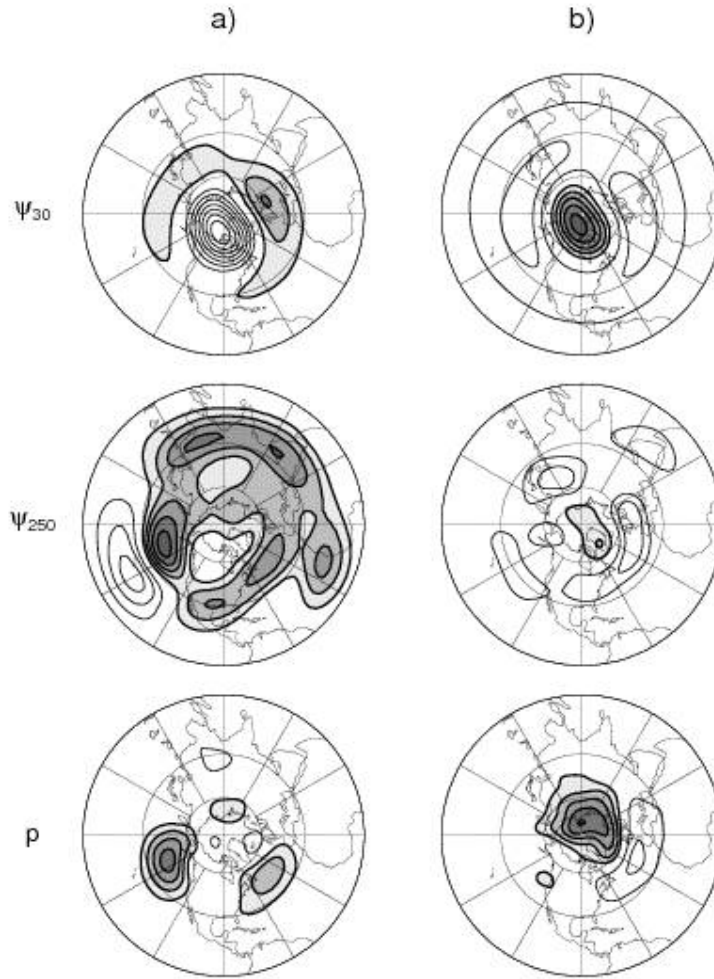


Figure 9. (Column a) Day 21 response to the tropical portion (30 S-30 N) of the optimal initial condition for maximizing the amplitude of $\psi_T/\text{EOF1}$. (Column b) Day 21 response to the extratropical portion (35N-90N) of the optimal initial condition for maximizing the amplitude of $p/\text{EOF1}$. The full optimal initial condition in both cases is normalized to unity. Contour intervals: Top row: 30 hPa streamfunction (ψ_{30} ; $3.75 \times 10^5 \text{ m}^2\text{s}^{-1}$). Middle row: 250 hPa streamfunction (ψ_{250} ; $2.5 \times 10^5 \text{ m}^2\text{s}^{-1}$). Bottom row: SLP (p ; 20 Pa). Positive values are indicated by shading and thick contours, and negative values by thin contours.

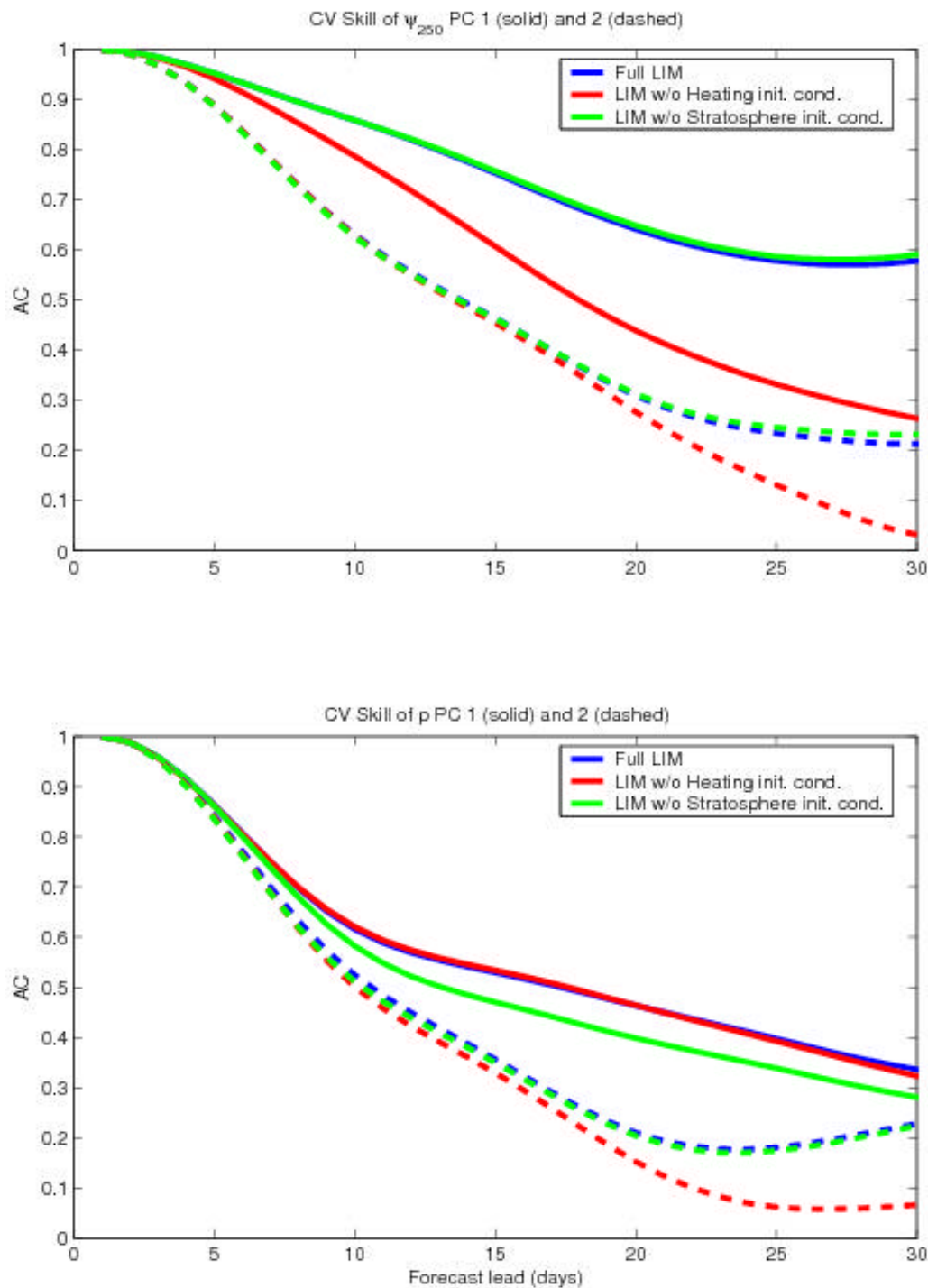
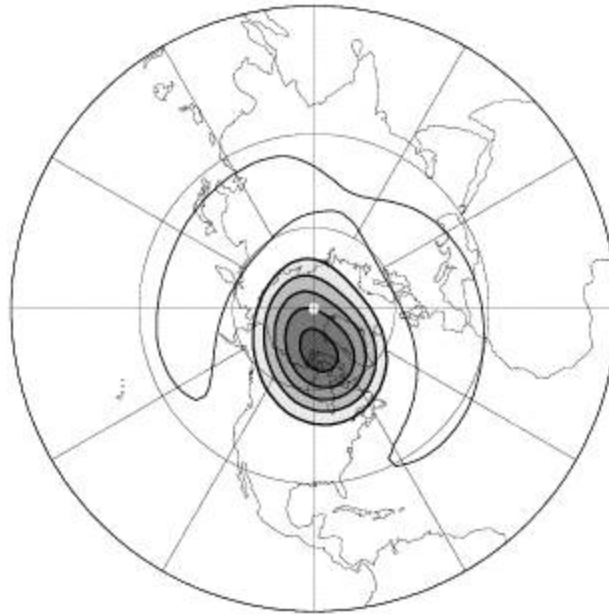


Figure 10. Forecast skill of leading SLP and tropospheric streamfunction PCs (blue lines), compared to skill obtained when either tropical heating (red lines) or stratospheric streamfunction (green lines) initial conditions are removed. All forecast skill is cross-validated. Note that the same linear operator is used to generate all three sets of forecasts. Top: skill for the two leading tropospheric streamfunction (ψ_T) PCs. Bottom: skill for the two leading SLP (p) PCs. In both panels, solid lines indicate PC 1 skill and dashed lines indicate PC 2 skill.

30 hPa streamfunction anomaly, Day 21



Initial heating anomaly

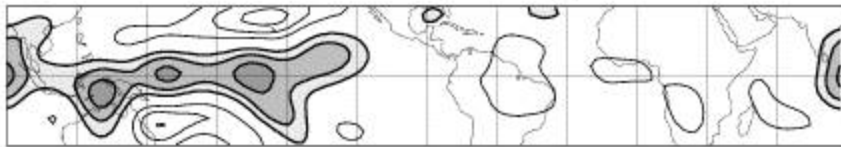


Figure 11. Day 21 30 hPa streamfunction response of the full LIM (top) to the initial tropical heating anomaly shown in the bottom panel. This heating pattern is taken from the optimal initial condition leading to maximum amplification of ψ_s /EOF2 over 21 days. Contour intervals are Top: $3.75 \times 10^5 \text{ m}^2\text{s}^{-1}$ and Bottom: $7.5 \times 10^{-3} \text{ PaKs}^{-1}$. Positive values are indicated by shading and thick contours, and negative values by thin contours.

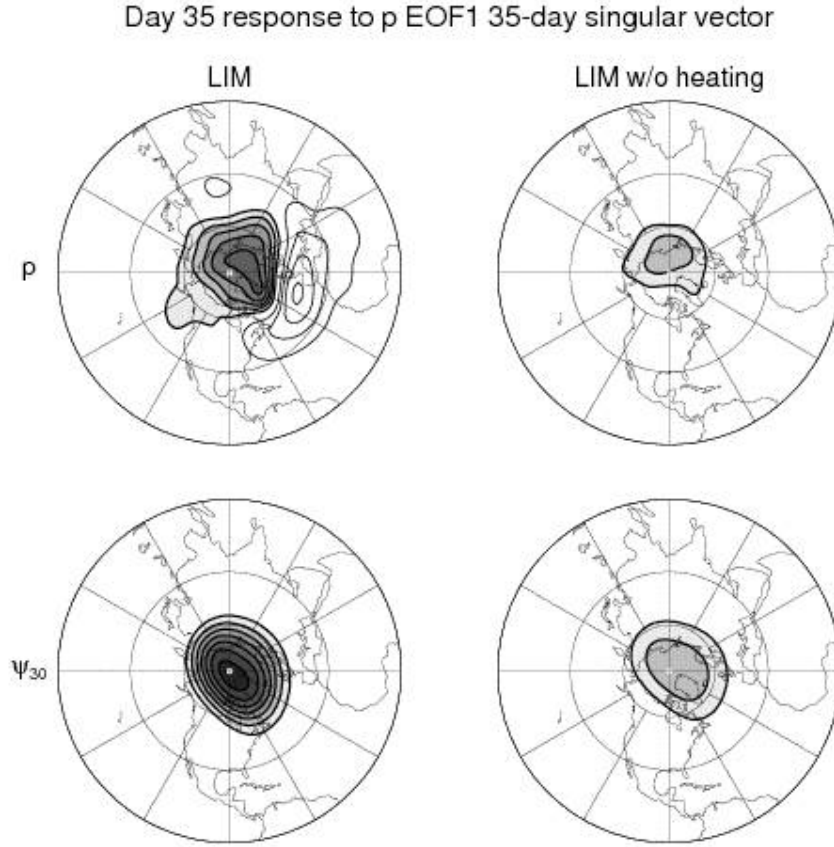


Figure 12. Day 35 \mathbf{p} (top) and ψ_{30} (bottom) response to the leading singular vector for a 35 day lag, where the norm is the amplification of the leading \mathbf{p} EOF. Left panels show anomalies evolved using the full LIM. Right panels show anomalies evolved without tropical influences; that is, evolved by \mathbf{L}_{noh} . Contour intervals are 10 Pa for the top row and $3.75 \times 10^5 \text{ m}^2 \text{ s}^{-1}$ for the bottom row. Positive values are indicated by shading and thick contours, and negative values by thin contours.

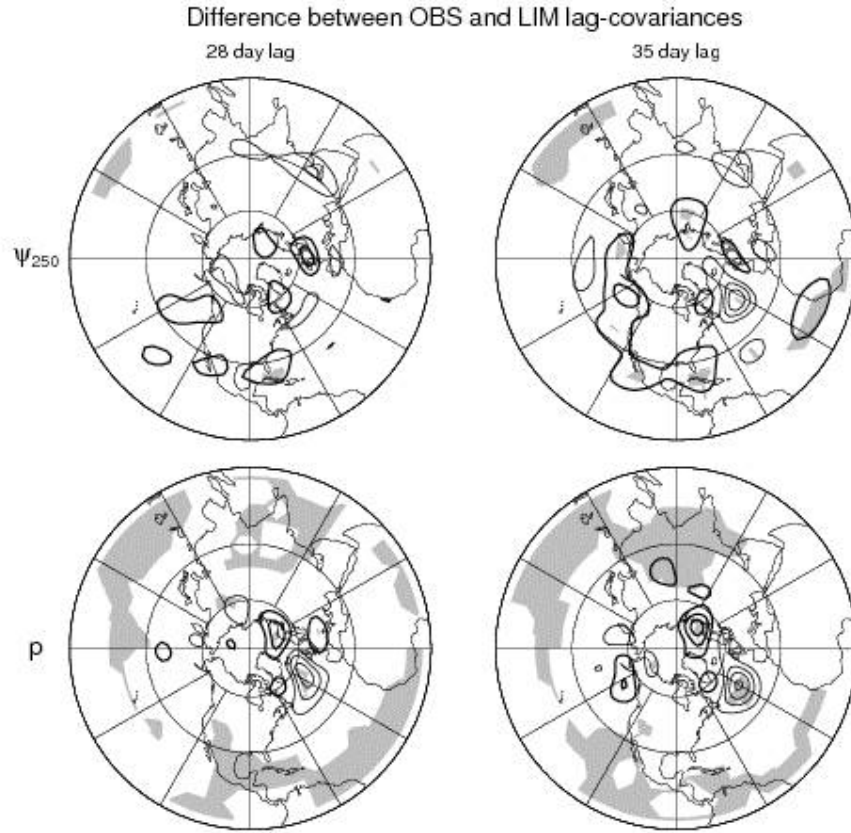


Figure 13. Difference between observed and LIM-predicted 28-day (left) and 35-day (right) lag-covariances, for ψ_{250} (top panels) and p (bottom panels). Positive values are indicated by thick contours and negative values by thin contours. Contour intervals are as in Fig 3. Gray shading indicates where the LIM lag-covariance does not lie within the 90% confidence interval for the observed lag-covariance, based on a Monte Carlo test; see text for more details.

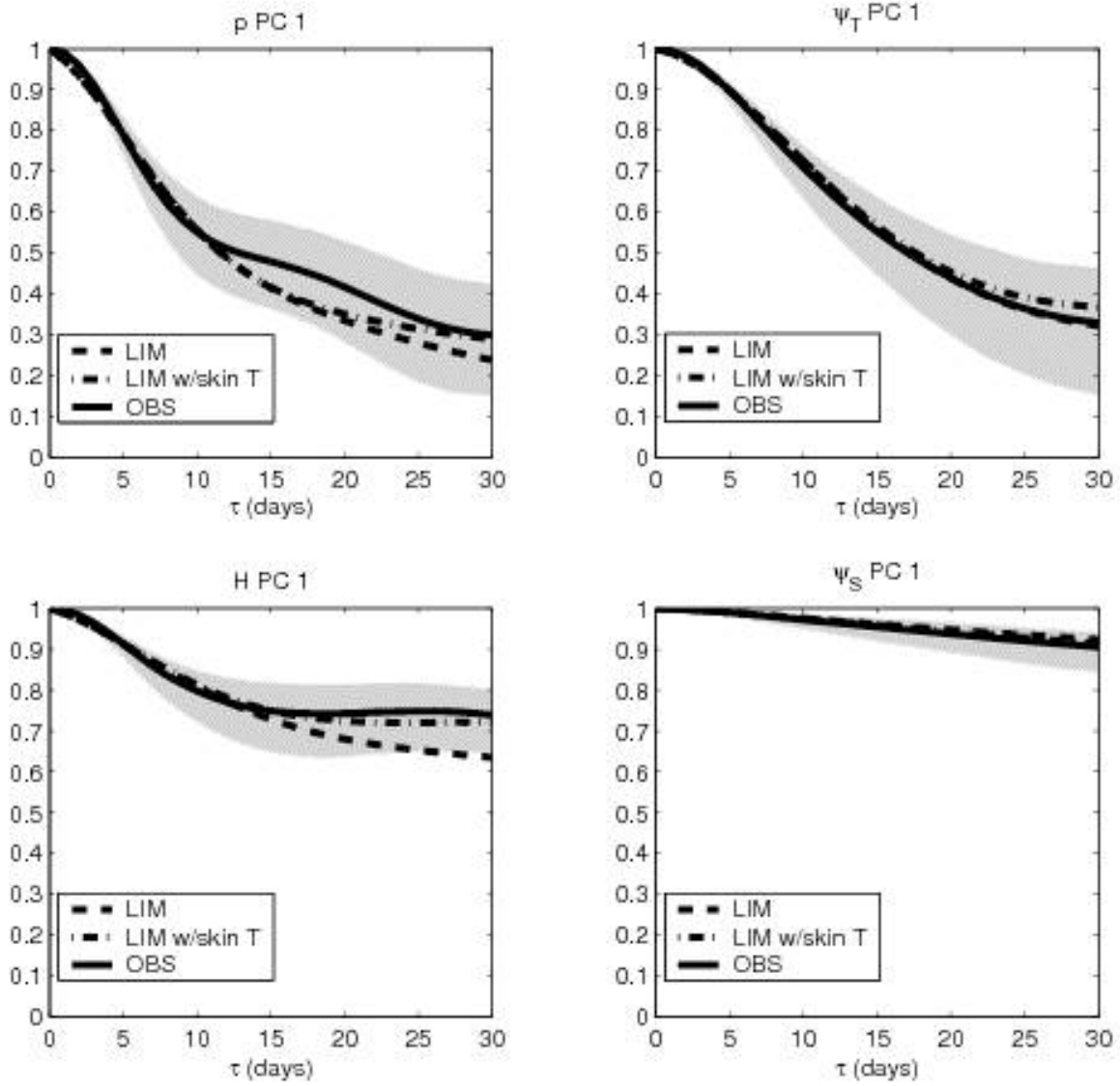


Figure 14. Comparison of the autocorrelation function of the leading principal component of each model variable, for observations (solid line) and the LIM (dashed line). Gray shading indicates the 90% confidence interval for the observed autocorrelation, based on a Monte Carlo test. Results obtained using an extended LIM with additional tropical oceanic skin temperature components are shown as dashed-dotted lines.